



A Pluto–Charon Concerto: An Impact on Charon as the Origin of the Small Satellites

Benjamin C. Bromley¹ and Scott J. Kenyon²

¹ Department of Physics & Astronomy, University of Utah, 115 S 1400 E, Rm 201, Salt Lake City, UT 84112, USA; bromley@physics.utah.edu

² Smithsonian Astrophysical Observatory, 60 Garden St., Cambridge, MA 02138, USA; skenyon@cfa.harvard.edu

Received 2019 November 1; revised 2020 June 2; accepted 2020 June 17; published 2020 July 30

Abstract

We consider a scenario where the small satellites of Pluto and Charon grew within a disk of debris from an impact between Charon and a trans-Neptunian object (TNO). After Charon’s orbital motion boosts the debris into a disk-like structure, rapid orbital damping of meter-sized or smaller objects is essential to prevent the subsequent reaccretion or dynamical ejection by the binary. From analytical estimates and simulations of disk evolution, we estimate an impactor radius of 30–100 km; smaller (larger) radii apply to an oblique (direct) impact. Although collisions between large TNOs and Charon are unlikely today, they were relatively common within the first 0.1–1 Gyr of the solar system. Compared to models where the small satellites agglomerate in the debris left over by the giant impact that produced the Pluto–Charon binary planet, satellite formation from a later impact on Charon avoids the destabilizing resonances that sweep past the satellites during the early orbital expansion of the binary.

Unified Astronomy Thesaurus concepts: Pluto (1267); Natural satellites (Solar system) (1089); Planet formation (1241); Kuiper belt (893); Trans-Neptunian objects (1705)

1. Introduction

The spectacular New Horizons flyby of Pluto and Charon has deepened the mystery surrounding the binary planet’s delicate system of satellites. With orbital periods close to resonances at 3:1 (Styx), 4:1 (Nix), 5:1 (Kerberos), and 6:1 (Hydra) times the 6.4 day period of the central binary, the satellites are as tightly packed as possible (e.g., Buie et al. 2006; Weaver et al. 2006; Tholen et al. 2008; Youdin et al. 2012; Brozović et al. 2015; Showalter & Hamilton 2015; Kenyon & Bromley 2019b, 2019c). Despite their intriguing orbits, the satellites seem like an afterthought, together accounting for less than 0.001% of Pluto’s mass. How these moons formed remains uncertain.

In the most popular formation model, the small moons arose from debris after the grazing collision that led to the formation of the Pluto–Charon binary (Canup 2005, 2011; Asphaug et al. 2006; Ward & Canup 2006; Desch 2015; McKinnon et al. 2017). While this event ejects enough material to make the small moons, the central binary probably acquires an eccentric orbit with a period of 1–2 days soon after the collision. Driven by tidal interactions, the orbits of Pluto and Charon circularize and drift apart with time. As the binary expands, the locations of $n:1$ resonances with the binary orbit sweep outward and destabilize circumbinary material (e.g., Lithwick & Wu 2008b; Cheng et al. 2014b; Smullen & Kratter 2017; Woo & Lee 2018). Although collisional damping and gravity-driven viscosity might stabilize small particles within resonances (Bromley & Kenyon 2015), it is not clear whether these particles can collide and merge into larger satellites that remain on stable orbits as the central binary evolves.

In another scenario, Charon grows within a massive debris swarm produced from a collision with Pluto that largely destroyed the impactor (Canup & Asphaug 2001; Canup 2005; Kenyon & Bromley 2019a). As with a grazing collision, the debris from the impact provides a reservoir for the small satellites. Again, uncertainties in the subsequent evolution of the system allow only speculation that the four moons could survive the tidal expansion of the binary.

Here, we explore the idea that the satellites grew out of debris from a giant impact well after the binary planet settled into its present configuration. In this picture, ejecta from a collision between a trans-Neptunian object (TNO) and Charon forms a flattened, highly eccentric, circumbinary swarm of solids. The challenge is to find a mechanism that rapidly damps the orbits of debris particles before they are accreted or ejected by the binary. After reviewing the Pluto–Charon system (Section 2), we provide analytical estimates to compare different mechanisms for dynamically cooling debris orbits (Section 3), bolstered by simulations of disk evolution with the hybrid n -body–coagulation code, *Orchestra* (Section 4). Then, in Section 5, we use our results to specify broad requirements for the successful production of the small moons by an impact with Charon. Our conclusions are in Section 6.

2. Preliminaries

Today, the small satellites of Pluto and Charon lie on nearly circular orbits in the plane of the binary at distances between $35R_p$ and $55R_p$ from the barycenter, where $R_p = 1188$ km is Pluto’s radius (Stern et al. 2015, 2018). We define a “satellite zone” that encompasses these orbits, an annular region extending from $33R_p$ to $66R_p$ around Pluto–Charon’s center of mass, a range that is equivalent to two to four times the binary separation, $a_{\text{bin}} \approx 16.5R_p \approx 19,600$ km. The midplane of this zone coincides with the orbital plane of the central binary and the satellite system. Interior to this zone, prograde, coplanar orbits around the binary are unstable (e.g., Dvorak et al. 1989; Holman & Wiegert 1999; Doolin & Blundell 2011; Youdin et al. 2012; Gaslac Gallardo et al. 2019; Kenyon & Bromley 2019b). Styx, near the inner edge of the satellite zone, seems unnervingly close to this unstable region. Figure 1 and Table 1 together summarize the present-day configuration of the satellite system.

The mass in the satellite zone is at least the sum total of the masses of the four satellites, M_{snkh} . On the basis of Hubble Space Telescope and New Horizons observations (Weaver et al. 2006, 2016; Showalter et al. 2011, 2012; Brozović et al. 2015),

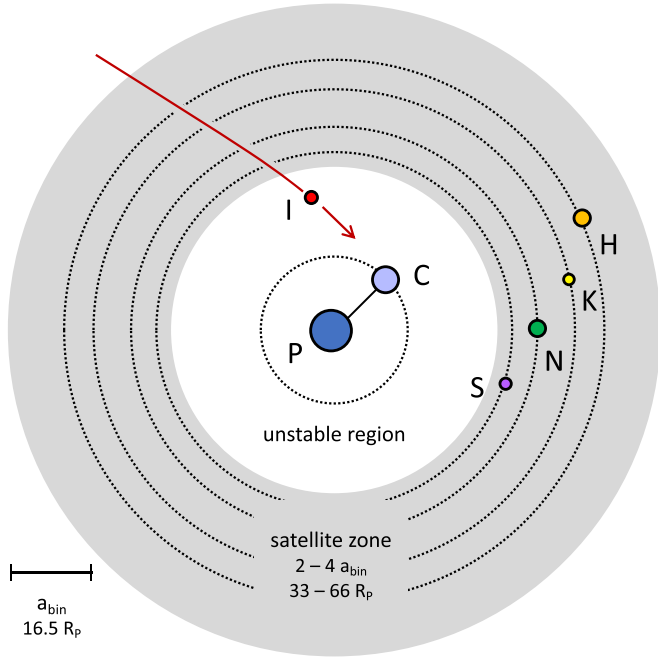


Figure 1. Schematic of the Pluto–Charon satellite system with a hypothetical trans-Neptunian impactor. Orbits are to scale, while sizes of symbols are only suggestive of physical sizes: “PC” are the binary, “SNKH” are the small satellites, and “I” designates an impactor that may scatter debris into the satellite zone. Debris particles that manage to settle on orbits in the unstable region are ejected or accreted by the binary.

Table 1
Nominal Properties of the Pluto–Charon System^a

Name	Mass (kg)	Radius (km)	a/a_{bin}	a/R_p	Period (days)
Pluto	1.303×10^{25}	1188	6.39
Charon	1.587×10^{24}	606	1	16.49	6.39
Styx	$\lesssim 5 \times 10^{18}$	5.2	2.178	35.94	20.2
Nix	45×10^{18}	19.3	2.485	41.02	24.9
Kerberos	$\lesssim 16 \times 10^{18}$	6	2.949	48.681	32.2
Hydra	48×10^{18}	20.9	3.303	54.54	38.2
Satellite zone	1.2×10^{20}	(>30)	1–2	33–66	17.8–51.0

Note.

^a See Brozović et al. (2015), Stern et al. (2015), Weaver et al. (2016), Nimmo et al. (2017), McKinnon et al. (2017), and Kenyon & Bromley (2019c).

along with dynamical studies (Youdin et al. 2012; Showalter & Hamilton 2015; Kenyon & Bromley 2019c), we adopt $M_{\text{snkh}} = 1.2 \times 10^{20}$ g, the mass of a modest-size (30 km) icy body (Table 1). This estimate provides a guideline for establishing the mass that must be delivered to the satellite zone by a major collision with the binary.

Our goal here is to assess whether an impact between a TNO and the Pluto–Charon binary leads to the formation of the four satellites. We focus on Charon as the target because its orbital motion helps boost impact debris into a prograde circumbinary disk (Section 3). We assess how efficiently mass from an impact is delivered to the satellite zone (Section 3) and how it settles there in a dynamically cool disk (Section 4). These calculations inform the mass of the impactor and the impact geometry (Section 5). If the impact is a direct hit, as in a cratering event, then the estimated projectile mass is roughly

ten times M_{snkh} , corresponding to a ~ 100 km TNO. A smaller projectile may deliver enough material directly to the satellite if its impact is a well-aimed, surface-skimming event (Leinhardt & Stewart 2012), beaming debris into a prograde orbit. In any case, material launched into the satellite zone must somehow settle there. We place constraints on this process next.

3. Formation of a Circumbinary Disk

An impact between a TNO and either Pluto or Charon produces copious amounts of debris. In this section, we explore how this material is delivered to the satellite zone, and how it might settle onto stable orbits in the plane of the binary. The main results include estimates of debris particle sizes and total debris mass required to place enough material in the satellite zone for building Nix and its siblings. We begin with an argument that binary dynamics make it easier to deliver debris to the satellite zone, and that Charon is the better target for the TNO impact.

3.1. Impact Events On a Binary: Why Charon

An impact event on the surface of a single planet—as in Pluto before it was joined by Charon—can lead to a range of outcomes, depending on the impact parameter and impactor size, among other factors. In a simple scenario, the impact obliterates the projectile, kicking up many small debris particles that do not interact with each other. Particles moving faster than the planet’s escape speed are lost; slower-moving objects fall back onto the planet’s surface. Through ejection and accretion, all of the debris is gone in a dynamical time.

A binary partner like Charon changes this picture. Because both planets are in motion relative to the center of mass, they are not always easy targets for debris that falls back toward them. Instead, many debris particles make multiple close passes by the binary before being accreted or ejected. Debris particles also have significant angular momentum in the center-of-mass frame if they are launched from the surface of the secondary and are boosted by its orbital motion about the primary. The result is a disk-like swarm of debris, roughly aligned with the binary’s orbital plane, that survives much longer than the dynamical time.

The presence of a binary partner also determines how the spray of collision ejecta eventually settles into a disk. As seen in the early work of Brahic (1975, 1976), debris particles around a point mass will dynamical cool through collisional processes into a common midplane established by their total angular momentum. The presence of a massive binary partner like Charon produces tidal torques that coerce debris into the plane of the binary (e.g., Larwood & Papaloizou 1997; Foucart & Lai 2013), similar to the effect of Saturn’s axisymmetric potential on its thin, coplanar rings (Goldreich & Tremaine 1982). When impact debris is launched from the secondary, the net angular momentum of the spray of ejecta is already roughly aligned with that of the binary, facilitating the settling process as the debris orbitally damps. However, this mechanism only works if the debris disk can survive long enough to dynamical cool.

To estimate the production and survival of debris following an impact, we perform a suite of simulations with Pluto, Charon, and noninteracting tracer particles. We select 16 impact sites at random on the surface of each target and “eject” 5000 tracer particles in an idealized, hemispherical spray

pattern from each site. The ejection speed of each tracer, v_{ej} , defined relative to the target body, is drawn from a power-law distribution, $f(v > v_{ej}) \sim v_{ej}^{-\alpha}$, where $\alpha \approx 1-3$ (e.g., Gault et al. 1963; Stoeffler et al. 1975; O’Keefe & Ahrens 1985; Housen & Holsapple 2011), above some minimum speed v_{min} . Our choice, $\alpha = 2$, suggests an icy, nonporous target. We expect weaker, porous material to yield a flatter speed distribution, while a higher tensile strength steepens it (see Svetsov 2011; see also Kenyon et al. 2014). When Charon is the target, we use $v_{min} \approx 0.56 \text{ km s}^{-1}$, sufficient to reach Charon’s nominal Hill radius, $a_{bin}(M_C/3M_P)^{1/3} \approx 5.8R_P$.³ When the target is Pluto, $v_{min} \approx 1.1 \text{ km s}^{-1}$, enabling all tracers to reach the nearest point on Charon’s Hill sphere, roughly $10R_P$ from Pluto. With these choices, we track fast particles that travel directly to the satellite zone, as well as those that are scattered into it by close passes with the binary partners.

With positions and speeds assigned in this way, we evolve the binary and the tracers forward in time using the sixth-order n -body integrator within our *Orchestra* code (Bromley & Kenyon 2006, 2011a; Kenyon & Bromley 2008, 2016). For good temporal resolution, time steps range from 15 minutes to less than ten seconds when resolving close encounters and collisions. This resolution is important even for particles with semimajor axes in the satellite zone with month-long orbital periods; their eccentricities tend to be high, and they risk strong and quick encounters with Pluto or Charon with each pericenter passage.

The code can also simulate orbital damping, a feature we use to estimate the damping rates required to settle tracers on coplanar, circular orbits before repeated close encounters with the binary remove them (Bromley & Kenyon 2006). We implement damping by adjusting a particle’s angular momentum vector, without modification to orbital energy or phase. To shift eccentricity, the code changes the magnitude of the angular momentum, deriving new position and velocity vectors that preserve the direction of the Laplace–Runge–Lenz vector and orbital phase. The code implements a shift in inclination with a coordinate transformation that rotates the angular momentum vector toward or away from that of the binary.

We damp tracers only when they are in or beyond the satellite zone, since Keplerian orbital elements are not good measures of motion close to the binary. This feature is important for estimating the damping rates required to settle tracers on coplanar, circular orbits before repeated close encounters with the binary remove them.

We first consider cases with no orbital damping of the ejecta. Figures 2 and 3 display the results, showing the eccentricity and inclination of bound tracer particles as a function of semimajor axis at several snapshots in time when either Pluto (Figure 2) or Charon (Figure 3) is the impact target. The plots include the ejecta of multiple impacts; with a broad spray pattern, individual events yield phase-space distributions similar to the composite. In Figure 2, the tracers ejected from Pluto form a roughly spherical cloud, with polar orbits more prevalent than low-eccentricity, disk-like ones.

These orbits are hard to maintain. After ejection, tracers fall back close to Pluto, which readily scatters or accretes them. Those tracers that additionally lie in the plane of the binary may get removed by Charon.

In contrast, when debris particles are ejected from Charon, the orbits are more closely aligned with the orbital plane of the binary (Figure 3). The reason is that Charon’s orbital motion boosts the angular momentum of the ejected particles. The more numerous, slower-speed ejecta have specific angular momentum similar to Charon itself, yielding a thick, equatorial disk. The scale height can be inferred from Figure 3, which shows a concentration of inclinations around 25° . Tracers on these orbits are significantly longer-lived than their counterparts that were ejected from Pluto. We conclude that an impact on Charon sets the stage for the formation of the satellites, while impacts on Pluto do not.

3.2. Settling Into a Disk: General Requirements

Even when tracers are launched from Charon, the simulations show that, over a period of years, the bound particles return to the vicinity of the binary time and again until they are either accreted or ejected (Figure 3). Figure 4 emphasizes this point. The number of bound tracers in the simulations falls steeply in time; less than two percent of the initial tracer population remains after four years. With only the gravity of Pluto and Charon included in this calculation, we expect that all tracers will eventually be accreted or ejected.

Despite that bleak result, Figure 4 also provides hope that a reservoir of mass can be preserved to seed the formation of Pluto–Charon’s small satellites. The plot shows that orbital damping in eccentricity e and inclination i leads to a significant amount of debris on stable, bound orbits around the binary. For that demonstration, we adopt a constant timescale τ , damping the eccentricity and inclination of each tracer at a rate of e/τ and i/τ , respectively. Figure 4 indicates that a damping time of no longer than $\tau \sim 5 \text{ yr}$ is required to prevent a sizable fraction ($\gtrsim 10\%$) of the impact ejecta from being ejected or accreted.

Even in the cases of rapid damping, only $\sim 1\%$ of the total number of tracers settle in the satellite zone. However, the simple “in-place” damping mechanism, where e and i are steadily reduced around the osculating semimajor axis a , is not representative of realistic damping processes. Instead, collisional damping will concentrate particles where the local number density is high, which happens to be in the satellite zone (Figure 3). If the impact event generates a cloud of gas, aerodynamic drag can trap small particles wherever the gas is, even if they would otherwise be on unbound orbits. Then, as in Figure 4, as much as 20% of the material ejected beyond Charon’s Hill sphere might wind up in the satellite zone. We explore these damping mechanisms next.

3.3. Collisional Evolution

In a swarm of solid particles, collisions drive orbital damping. From basic kinetic theory, the average rate of collisions experienced by a particle with radius r in a sea of other similar particles scales as “ $n v \sigma$.” Applying this estimator to a thick disk of debris (as in Figure 3), the average time

³ This value gives roughly the average of Charon’s distance to the Lagrange points L1 and L2—we do not take into account the nonspherical shape of the Roche lobe. The goal here is simply to track particle orbits that do not have enough energy to reach the satellite zone directly but that might get scattered there by the binary.

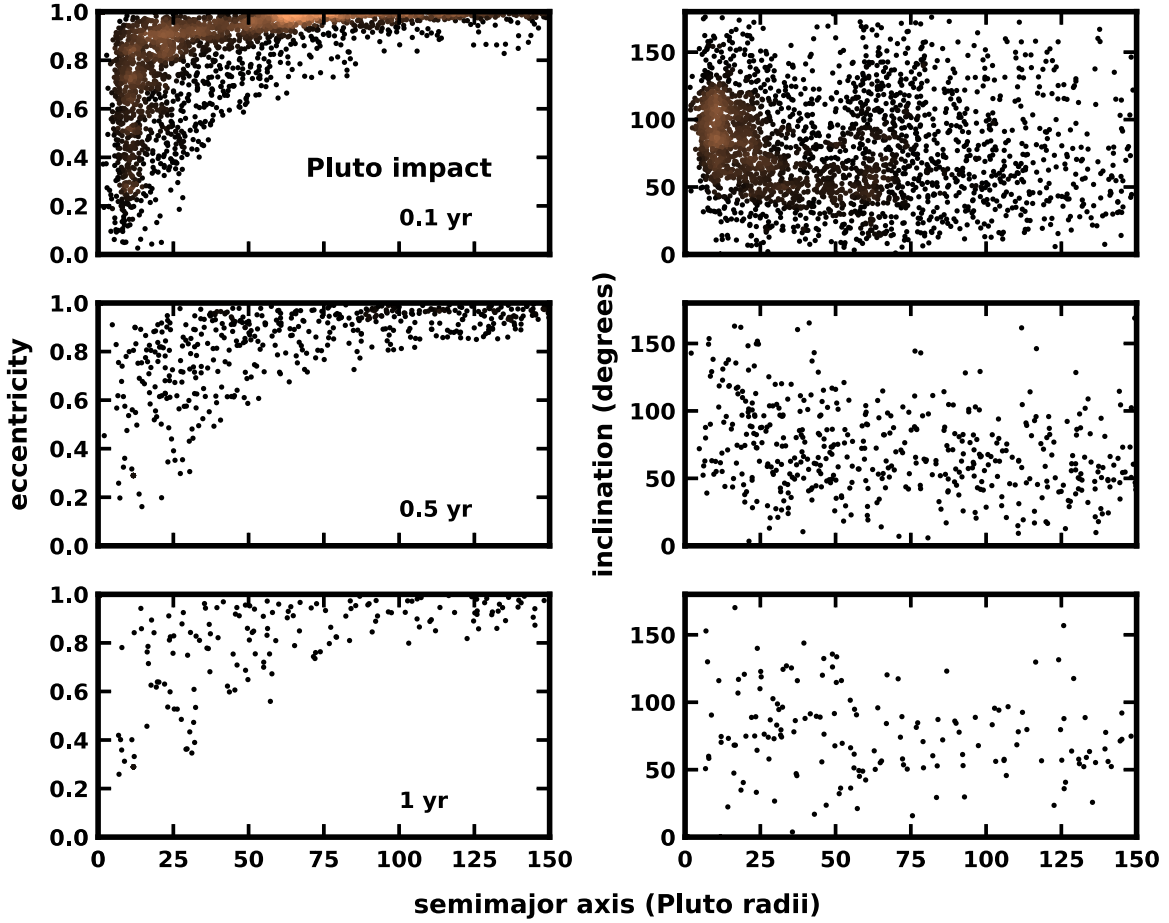


Figure 2. Eccentricity and inclination of particles representing impact ejecta from Pluto as a function of barycentric semimajor axis. Each row corresponds to a snapshot at a specific time after impact, as indicated in the left panels. Plots contain tracers from multiple impact events; since the adopted spray pattern of ejecta is broad, individual events yield similar distributions in this orbital parameter space. Marker color corresponds to local number density of points in each plot, to help distinguish regions where the markers overlap. For comparison, the same color map is used in Figure 3, where the density of points is higher. Left panels show that the eccentricity of bound particles is concentrated at values near unity, while the inclination (right panels) is broadly distributed. Repeated encounters with the binary rapidly remove particles from the system.

between collisions for each particle is

$$\begin{aligned}
 t_{\text{col}} &\sim \frac{4\pi\rho r^3 a_{\text{eff}}}{3\Sigma} \cdot \frac{1}{e_{\text{eff}} v_k} \cdot \frac{1}{4\pi r^2} \\
 &\sim 2.0 \times \left[\frac{\rho}{1 \text{ g cm}^{-3}} \right] \left[\frac{r}{10 \text{ m}} \right] \left[\frac{\Sigma}{1 \text{ g cm}^{-2}} \right]^{-1} \\
 &\quad \times \left[\frac{a}{50 R_P} \right]^{3/2} \left[\frac{t_{\text{eff}}}{25^\circ} \right] \left[\frac{e_{\text{eff}}}{0.7} \right] \text{ yr}, \quad (1)
 \end{aligned}$$

where ρ is the density of solids in the impact debris, Σ is the surface density of the debris, a is the semimajor axis, t_{eff} is the typical orbital inclination, and $H = a_{\text{eff}}$ is the scale height of the debris swarm. The term v_k in the denominator is the local circular speed as if Pluto–Charon were a single point mass, while e_{eff} is an effective eccentricity, so that the product $e_{\text{eff}} v_k$ characterizes the random motion of the swarm of impact debris particles. Here, we have also used a cross section of $4\pi r^2$, appropriate to a population of identical, hard spheres.

Equation (1) illustrates numerical values of the collision time for specific parameter choices. The fiducial value of $\Sigma = 1 \text{ g cm}^{-2}$ corresponds to a total mass in the satellite zone that is

comparable to M_{snkh} , assuming that the surface density scales as $\Sigma \sim a^{-1.5}$. Note that we otherwise do not consider variation in the surface density of the debris in the above estimate of the damping time; doing so would steepen the dependence of t_{col} on semimajor axis. For the effective eccentricity, we adopt $e_{\text{eff}} = 0.7$ on the basis of the tracer simulations. The product $e_{\text{eff}} v_k$ with this value is representative of the random speeds of tracers in the satellite zone.

Equation (1) predicts general trends in the collision time, such as the decrease in t_{col} with increasing number density of the debris particles. However, details of the particle orbits can affect the numerical estimates. For example, if all particles were launched from impact into a narrow eccentric ring, then their relative velocities would be smaller than the value in Equation (1), resulting in a longer collision time. Similarly, when debris is launched by an impact on the surface of a single planet, the bound ejecta will have little spread in eccentricity as a function of semimajor axis; see, e.g., Hyodo et al. (2017a, 2017b) for a giant impact on Mars that may have formed its moons, Phobos and Deimos. However, the ejecta launched from Charon have relatively large random relative velocities as compared to an eccentric ring or debris from a single planet; for an illustration, compare Figure 6 of Hyodo et al. (2017b) versus Figure 3 here.

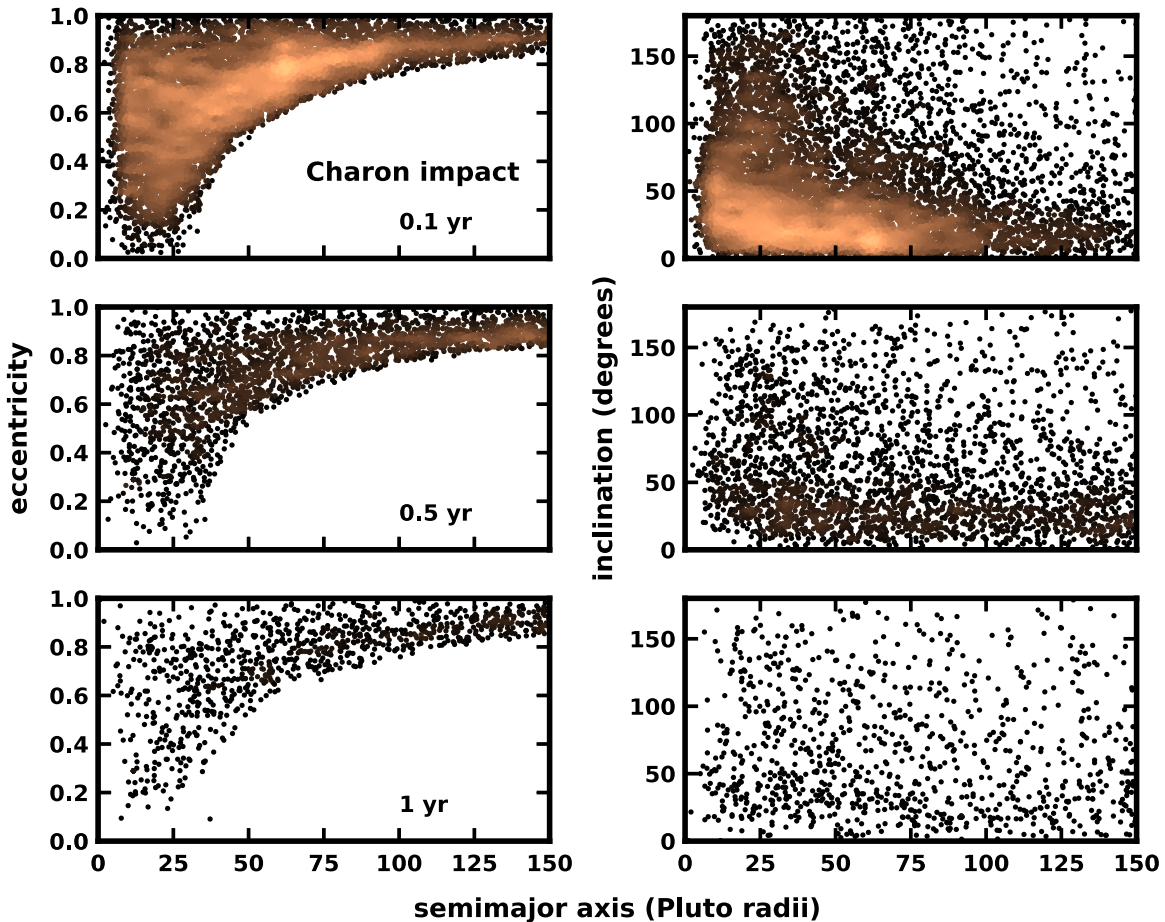


Figure 3. Eccentricity and inclination of particles representing impact ejecta from Charon, as in Figure 2. The typical eccentricity of ejecta is lower compared with impact ejecta from Pluto, and there is a stronger concentration of tracers with low-inclination orbits ($\sim 25^\circ$), showing presence of a thick disk. Because there is no orbital damping for the particles shown here, all will eventually get scattered or accreted by the binary. However, since particles in these simulations are launched with a velocity boost from Charon’s orbital motion, they survive longer than their counterparts in Figure 2.

Thus, we adopt Equation (1) as representative of a debris cloud with an origin on Charon’s surface.

3.3.1. Collision Outcomes

The collision time in Equation (1) sets the rate that collisional damping cools a dynamically hot population, causing it to settle into a thin, coplanar, circumbinary disk. Shortening t_{col} increases this rate. The details depend on the outcomes of myriad pairwise collisions—the amount of random kinetic energy lost, and whether particles erode or shatter in the process. The physics of inelastic collisions (e.g., Porco et al. 2008; Bromley & Kenyon 2015) and fragmentation is important. If particles are broken up as the debris swarm evolves, they become smaller but more numerous, significantly driving up the collision rate (Wetherill & Stewart 1993; Williams & Wetherill 1994; Tanaka & Ida 1996; Kenyon & Luu 1999a; O’Brien & Greenberg 2003; Kobayashi & Tanaka 2010).

To distinguish collision outcomes, we follow established theory by comparing the pairwise center-of-mass collision energy Q_c with the specific binding energy, Q_D^* (Davis et al. 1985; Housen & Holsapple 1990; Benz & Asphaug 1999; Leinhardt & Stewart 2012):

$$Q_c = v_{\text{rel}}^2/8, \text{ and } Q_D^* = Q_b r^{-0.4}, \quad (2)$$

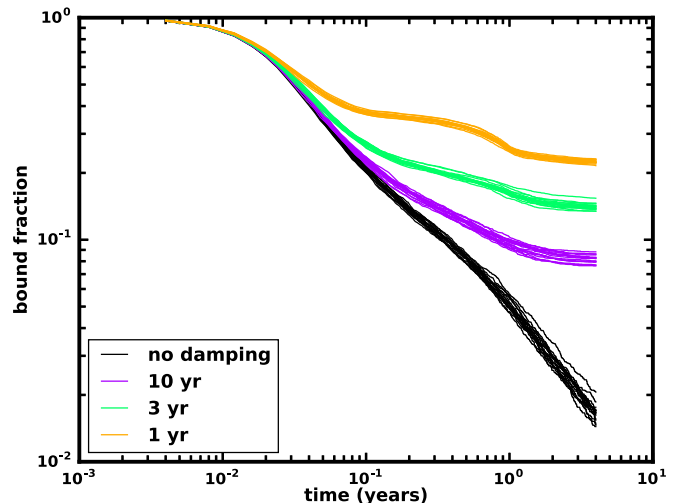


Figure 4. Survival fraction of all simulated ejected particles as a function of time since impact. Black curves show the fraction of bound tracers for individual impact events. Lighter-colored curves correspond to runs with eccentricity and inclination damped on timescales as indicated in the legend. When damping times are much longer than a few years, less than 10% of the tracers remain. In all cases, the number of particles in the satellite zone is only about 10% of the survivors. Less than a few percent of the total number of tracers remain in the satellite zone.

where the expression for Q_c applies to equal-mass bodies (Kenyon & Bromley 2014) and Q_b is a material-dependent strength constant. This form of Q_D^* applies to smaller bodies ($r \lesssim 0.1$ km) for which self-gravity is unimportant (e.g., Leliwa-Kopystyński et al. 2016). Particles are stronger when they are smaller because they are less susceptible to internal fractures than their larger counterparts. We set $Q_b = 2 \times 10^6$ erg/g cm^{0.4}, acknowledging that literature values range from an order of magnitude lower (Leinhardt et al. 2008; Leinhardt & Stewart 2009; Schlichting et al. 2013) (“weak ice”) to an order of magnitude higher (Benz & Asphaug 1999) (“strong ice”) than our choice (“ice”).

By setting $Q_D^* = Q_c \sim v_k^2/8$, we solve for the radius of particles that marks the transition between disruptive and inelastic collisions,

$$r_D^* = (Q_c/Q_b)^{5/2} \sim 0.017 \times \left[\frac{e_{\text{eff}}}{0.7} \right]^{-5} \left[\frac{a}{50R_p} \right]^{5/2} \left[\frac{Q_b}{2 \times 10^6 \text{ erg/g cm}^{0.4}} \right]^{5/2} \text{ cm.} \quad (3)$$

Particles smaller than r_D^* are able to grow into larger objects as a result of collisions, while large objects lose mass.

This threshold value of particle radius is sensitive to the semimajor axis and the assumed particle tensile strength. Weak ice has a disruption radius of about $0.4 \mu\text{m}$. Strong ice has a disruption radius of a few centimeters. The threshold radius is even more sensitive to the effective eccentricity of the debris swarm; r_D^* increases dramatically as e_{eff} is reduced, since smaller eccentricities mean lower collision speeds that allow larger particles to survive. Thus, velocity evolution is key to the swarm’s ultimate size distribution.

3.3.2. A Simple Evolution Model

Guided by detailed simulations showing that a collisional cascade can produce rapid damping (Kenyon & Bromley 2014), we use an idealized picture to discern trends in the evolution of the swarm’s velocities and size distribution. An initial debris swarm consisting of identical particles experiences a round of collisions in time $t_{\text{col}} = t_0$, breaking up all bodies into more numerous smaller ones. This next generation of debris has both a higher space density and slower random motions, which together affect the next round of collisions. With each generation, velocities damp and orbits circularize. In the early stages, when particle sizes and collision speeds are large, disruptive collisions churn bigger bodies into many smaller ones. Eventually, as random motions become small, collisions become inelastic with little fragmentation. The surviving particles settle into a thin disk on coplanar, most circular orbits about the binary planet (Lee & Peale 2006; Youdin et al. 2012; Bromley & Kenyon 2015).

To quantify how velocity and particle size evolve in this scenario, we assume that, with each successive generation of shattering collisions, the radii of particles are reduced to a small fraction f of their previous size. A factor g gives the corresponding reduction in typical collision speed (or equivalently, e_{eff}). Once particle sizes and velocities are reduced so that particles just bounce off each other, $f \rightarrow 1$ and $g \rightarrow g_b$, where g_b is a damping factor related to the material-dependent coefficients of restitution (e.g., Bridges et al. 1984; Supulver et al. 1995). Armed with this prescription, along with the

collision time in Equation (1), we quantify the collisional evolution of the system.

If r_0 and e_0 are the radius and effective eccentricity of the initial swarm, then after n generations of disruptive collisions, particles have typical sizes $f^n r_0$ and speeds $g^n e_0 v_k$. The collision time between generations scales as r/v ; thus,

$$t_{\text{col}} = t_0 \left(\frac{f}{g} \right)^n, \quad (4)$$

where t_0 is the initial, post-impact collision time. The number of generations, n , if treated formally as a continuous function of time, is

$$n(t) = \text{floor} \begin{cases} \log[1 - (1 - f/g)t/t_0] / \log(f/g) & (f \neq g) \\ t/t_0 & (f = g) \end{cases}, \quad (5)$$

where $t = 0$ is the time of the formation of the debris swarm, and “floor” indicates the nearest lower integer. In general, when the ratio f/g is less than one, the collision time gets smaller with each generation. Otherwise (as is the case for bouncing collisions), the collision time grows.

What ultimately matters to the survival of the swarm around the Pluto–Charon binary is the damping time. From our tracer simulations (e.g., Figure 4), orbital damping times must be shorter than a decade to preserve a substantial reservoir of mass for the satellite system. Here, we define the damping time as

$$t_{\text{damp}} \sim \frac{e_{\text{eff}}}{de_{\text{eff}}/dt} \sim \frac{t_{\text{eff}}}{dt_{\text{eff}}/dt} \sim t_{\text{col}}/(1 - \tilde{g}), \quad (6)$$

where \tilde{g} is either the velocity factor g_b for bouncing collisions or g for collisions that are disruptive. While values of g and g_b are uncertain (for examples involving coefficients of restitution for water ice, see Gärtner et al. (2017) and references therein), we recommend values well below 0.5. This range acknowledges that, in high-speed disruptive collisions, much of the kinetic energy is dissipated as heat. In bouncing collisions, heat, compactification, and cratering damp rebound speeds (see Porco et al. 2008, Figure 22 therein). Thus, t_{damp} is 1–2 times t_{col} . Within a few generations of collisions, orbits are fairly circular and the debris is safe from close encounters with the central binary. We consider specific scenarios next.

3.3.3. Large Debris Particles, Disruptive Collisions

If debris particles are initially large ($r \gg r_D^*$), the first generations of collisions grind them down to small sizes. From Equation (5), the number of generations required until shattering stops and the swarm particles reach their final size is:

$$n_{\text{cc}} \sim [11 + \log(r_0/10 \text{ m}) + 5 \log(e_0/0.7) - (5/2) \log(a/50R_p \cdot Q_b/Q_b')] / |\log(f) + 5 \log(g)|, \quad (7)$$

where Q_b' is our fiducial value (2×10^6 cgs), and we have assumed that both f and g are less than or equal to one; the subscript “cc” is a reference to “collisional cascade.” Setting $f = g = 0.5$ for a swarm of particles with $r_0 = 10$ m, it takes just three generations for the eccentricity to fall below 0.1 and for the particles to reach their final size of about 1 m. Still, the damping time is twice the collision time, so that with a mass M_{snkh} in the satellite zone (as in Equation (1)), three generations

takes about a decade. As in Figure 4, more than 90% of the debris will be lost to interactions with the binary in this time. A substantially more massive disk ($\gtrsim 10 M_{\text{snkh}}$ in the satellite zone), a smaller initial radius (< 10 m), or (as we expect) lower values of f and g would help to speed up damping and preserve more material in the satellite zone.

3.3.4. Small Debris Particles, Bouncing Collisions

Mutual collisions between submillimeter particles are inelastic, resulting in reduced random speeds and little change in particle sizes. Because particles are small and their number density is high even when the satellite zone has only the minimum mass needed to account for the satellites, collision times are very short. For example, a swarm of strong ice, made of “indestructible” particles as large as a few centimeters, has a collision time of less than a day. Even if coefficients of restitution are large (~ 0.5), the time to damp from $e_{\text{eff}} \approx 0.7$ to less than 10% of that value is months, not years. In general, we expect a swarm of small debris particles to damp and circularize quickly and efficiently.

Small particles, particularly the submicron grains of radii r_D^* for weak ice, may be lost to solar wind and radiation pressure (e.g., Pires dos Santos et al. 2013; Gaslac Gallardo et al. 2019). A debris swarm is protected from these and other effects if it is optically thick. We measure the optical depth of debris in the satellite zone in the vertical and radial directions, along rays that go through the plane of the thick disk, and along a path from the binary center of mass outward through the disk’s equatorial plane:

$$\tau_z = \frac{3\Sigma}{4\rho r} \sim 0.75 \times \left[\frac{\Sigma}{1 \text{ g cm}^{-2}} \right] \left[\frac{r}{1 \text{ cm}} \right]^{-1} \left[\frac{\rho}{1 \text{ g cm}^{-3}} \right]^{-1} \quad (8)$$

$$\tau_r = \frac{3\Delta a \Sigma}{4\rho r a_{\text{eff}}} \sim 1.1 \times \left[\frac{\Delta a}{33R_p} \right] \left[\frac{\Sigma}{1 \text{ g cm}^{-2}} \right] \times \left[\frac{r}{1 \text{ cm}} \right]^{-1} \left[\frac{\rho}{1 \text{ g cm}^{-3}} \right]^{-1} \left[\frac{a}{50R_p} \right]^{-1} \left[\frac{t_{\text{eff}}}{25^\circ} \right]^{-1}. \quad (9)$$

Particles smaller than roughly a centimeter thus form an optically thick cloud, conferring protection from significant losses from solar radiation.

We conclude that collisional damping, accelerated by a collisional cascade, is an effective means to rapidly damp a swarm of ejecta from a TNO-Charon impact, provided that the debris particles are numerous and small enough. If the typical debris particle is less than ~ 10 m in radius, and if there is more than $\sim M_{\text{snkh}}$ worth of debris in the satellite zone, then collisional damping leads to the formation of a circumbinary disk at the right location for building the satellites.

3.4. Damping in a Gas Cloud

If a circumbinary gas cloud forms during an impact, gas drag may be a source of orbital damping. We explore how such a cloud might affect the orbital dynamics of the solid debris. First, we consider preliminaries. The sound speed in the gas is

$$c_s = \sqrt{\frac{\gamma kT}{\mu_{\text{mol}} m_H}} \approx 0.15 \left[\frac{T}{40 \text{ K}} \right]^{1/2} \left[\frac{\mu_{\text{mol}} m_H}{18} \right]^{-1/2} \text{ km s}^{-1}, \quad (10)$$

where we let $\gamma = 1.3$ and molecular weight $\mu_{\text{mol}} = 18$, corresponding to water. This speed is comparable to the orbital

speed in the middle of the satellite zone, $v_k \approx 0.13 \text{ km s}^{-1}$ at $50R_p$. The mean thermal speed is larger, $v_{\text{therm}} \approx 1.4c_s$. We choose our fiducial temperature, $T = 40 \text{ K}$, to be roughly the equilibrium temperature at Pluto–Charon’s orbital distance from the Sun.

The temperature of the gas cloud is coupled with the cloud’s structure and fate around the central binary. The thickness of a gas disk around a central mass scales as c_s/v_k times the orbital distance (e.g., Shakura & Sunyaev 1973; Lynden-Bell & Pringle 1974). Even at $T = 40 \text{ K}$, and despite the angular momentum imparted to it from the Charon impact, the gas is too hot to settle into a disk. The sound speed is also close to the escape speed, $v_{\text{esc}} \approx 0.18 \text{ km s}^{-1}$ at $a = 50R_p$, indicating that the gas cloud will evaporate within a few dynamical times. Thus, we picture a scenario where the gas forms a short-lived, roughly spherical, rotating cloud.

Assigning a fiducial mass in gas of $M_{\text{gas}} = 10^{19} \text{ g}$, distributed uniformly in a spherical shell that spans the satellite zone, the mean free path of gas molecules is

$$\lambda \approx \frac{\mu_{\text{mol}} m_H}{\pi r_{\text{mol}}^2 \rho_{\text{gas}}} \approx 24 \left[\frac{\mu_{\text{mol}} m_H}{18} \right] \left[\frac{M_{\text{gas}}}{10^{19} \text{ g}} \right]^{-1} \left[\frac{r_{\text{mol}}}{0.3 \text{ nm}} \right]^{-2} \text{ m}. \quad (11)$$

This parameter helps to set how solid bodies interact with the gas. When a small debris particle of radius $r \lesssim \lambda$ has a speed v_{rel} relative to the gas, the drag force decelerates the particle at a rate of

$$a_{\text{drag}} \approx \frac{C_{\text{Eps}} \rho_{\text{gas}}}{\rho r} (v_{\text{therm}} + v_{\text{rel}}/4) v_{\text{rel}}, \quad (12)$$

where the constant $C_{\text{Eps}} = 1$ for specular reflection and is generally near unity for elastic collisions (Whipple 1972; Adachi et al. 1976; Weidenschilling 1977; Rafikov 2004). In the limit of slow particle speed ($v_{\text{rel}} \ll v_{\text{therm}}$), this expression is the Epstein drag law. The high speed limit ($v_{\text{rel}} \gg v_{\text{therm}}$) derives from a simple ballistic approximation where all molecules have a constant velocity in the frame of the macroscopic body. Interpolation between these two extremes gives us an estimate for cases relevant here, with $v_{\text{rel}} \sim v_{\text{therm}}$.

In a tenuous gas with $v_{\text{rel}} \approx v_{\text{therm}} \approx v_k$, the magnitude of the drag acceleration of a debris particle in the satellite zone scales roughly as v_k^2 . Thus, the “stopping time,” which characterizes the impact of gas drag on the dynamics of a solid particle, is

$$t_{\text{stop}} \equiv \frac{v}{a_{\text{drag}}} \sim \frac{\rho r}{\rho_{\text{gas}} v_{\text{rel}}} \sim 16 \left[\frac{\rho}{1 \text{ g cm}^{-3}} \right] \left[\frac{r}{1 \text{ mm}} \right] \left[\frac{M_{\text{gas}}}{10^{19} \text{ g}} \right]^{-1} \left[\frac{a}{50R_p} \right]^{3/2} \text{ days}. \quad (13)$$

The length of time in the lower equation is comparable to the dynamical time of orbits in the satellite zone. If the gas cloud is 10% of the mass of the present day satellites, then particles much smaller than 1 mm are entrained in the gas. Much larger objects do not notice the cloud.

From these results, there may be a pathway for the formation of a debris disk in the satellite zone. If the conditions are right for a collisional cascade, then much of the impact debris will be quickly converted into submillimeter grains and entrained in a rotating gas cloud. As the cloud evaporates and particles settle to the midplane, the solids form a thin disk with enough mass to move independently of the gas. Once the cloud vanishes, the remaining solids are free to coagulate and grow, as in a circumstellar planetary system.

However, the plausibility of this scenario depends on a number of uncertain factors, including the way the gas orbits the binary and how it disperses. For example, if the gas rotation is much slower than the local Keplerian speed, entrained solids will simply fall into the binary after the gas disperses. Otherwise, the presence of a cloud might help retain solid material that would have been removed by interactions with the binary.

3.5. Trapping Mass in the Satellite Zone

In our tracer simulations of an impact on Charon, orbital damping saves as much as 20% of debris particles from ejection or accretion by the binary. However, precious little of the ejecta ends up in the satellite zone when particles damp “in place,” even if they do so very quickly. Fortunately, significantly more mass likely ends up in the satellite zone than settles there in our tracer simulations. After a few binary orbits, about 3% of the total number of tracers have semimajor axes in the satellite zone, and over 10% have orbits that will pass into it. Collisions between these objects, along with others that are scattered into the satellite zone at different times, can trap material there. In this way, the mass in the satellite zone can be increased substantially.

Ejected debris crossing into the satellite zone will probably settle there if it participates in the collisional cascade at all. Solids orbiting interior to the satellite zone have short collision times and may be part of a robust collisional cascade closer to the binary (Equation (1)), but the strong dynamical excitation by the binary prevents settling. Instead, eccentricity pumping pushes debris particles into the satellite zone, where they are swept up by collisions with other debris there. While these trapping mechanisms will have some impact on the distribution of mass and angular momentum of stable material within the satellite zone, we anticipate that they are effective in trapping virtually all of the small debris particles that stray into the satellite zone. Thus, as much as 10% of the impact debris ejected beyond Charon’s Hill sphere can wind up in the satellite zone as mass available to build Hydra and company.

If trapping is necessary to increase the mass in the satellite zone to equal M_{snkh} , then the bulk of the debris particles must start off small, with a collision rate high enough to trigger the cascade. Assuming that the satellite zone can trap roughly three times the mass that it contains just after ejecta reaches it, then it might start out with a mass of only $0.3M_{\text{snkh}}$. Then, from Equation (1), the starting radius must be no larger than a few meters. In a debris swarm like this, the collisional cascade and trapping conspire to triple the mass in the satellite zone, delivering exactly the right amount for the satellites.

Many of the larger bodies that are not caught up in the collisional cascade pass into or completely through the satellite zone and may get trapped by the smaller debris that is forming a disk there. Trapping mechanisms include (i) dynamical friction between large impact fragments and gas (Ostriker 1999)

or small debris (e.g., Goldreich et al. 2004), (ii) kinematic friction caused by collisions with the small solids already settled in the satellite zone, and (iii) erosion of an interloper by the small debris. From analytical estimates (e.g., Ostriker 1999; Bromley & Kenyon 2014), the first mechanism—dynamical friction—is too slow-acting to be relevant in a scenario where rapid damping is essential. Thus, we focus on kinematic friction and erosion.

To explore these possibilities, we assume that the satellite zone contains a disk of small (<1 cm) particles with a total mass of 10^{20} g, spread uniformly across the disk with a typical inclination of $i_{\text{eff}} = 5^\circ$. A large body, with pericenter close to the binary, apocenter well beyond the satellite zone, and an inclination that is also around i_{eff} , passes through the satellite zone on a nearly radial path. As it does so, it experiences a loss of orbital energy given by the ballistic limit of Equation (12). By substituting gas density with that of the debris, and ignoring the debris particles’ thermal (random) motion, the energy change is

$$\Delta E \sim -\frac{\tilde{v}_{\text{rel}}^2}{\tilde{\rho}\tilde{r}} \frac{\Delta a \Sigma}{a i_{\text{eff}}}, \quad (14)$$

where \tilde{r} , $\tilde{\rho}$, and \tilde{v}_{rel} all refer to the large body. This loss of energy translates into a change of semimajor axis,

$$\frac{d\tilde{a}}{dt} \sim 2 \times \frac{\Delta E}{\pi} \sqrt{\frac{\tilde{a}}{GM}}, \quad (15)$$

where the factor of two accounts for energy loss during both inward and outward passages through the satellite zone. An estimate of the orbital decay time is then

$$\begin{aligned} t_{\text{decay}} &= \frac{\tilde{a}}{d\tilde{a}/dt} \approx \frac{\pi \tilde{\rho} \tilde{r} a i_{\text{eff}} \sqrt{GM\tilde{a}}}{2 \Sigma \Delta a v_{\text{rel}}^2} \\ &\approx 4.3 \times \left[\frac{\tilde{\rho}}{1 \text{ g cm}^{-3}} \right] \left[\frac{\tilde{r}}{10 \text{ m}} \right] \left[\frac{\Sigma}{1 \text{ g cm}^{-2}} \right]^{-1} \left[\frac{\Delta a}{33 R_{\text{P}}} \right]^{-1} \\ &\quad \times \left[\frac{a}{50 R_{\text{P}}} \right]^2 \left[\frac{i_{\text{eff}}}{5^\circ} \right] \left[\frac{\tilde{a}}{100 R_{\text{P}}} \right]^{1/2} \left[\frac{\tilde{v}_{\text{rel}}}{v_{\text{K}}} \right]^2 \text{ yr}, \end{aligned} \quad (16)$$

where we assume that the speed of the body relative to the swarm is approximately the local circular speed in the satellite zone. If the interloping body has a higher inclination than i_{eff} , the decay time is substantially longer. A body on an eccentric orbit that lies well out of the plane of the disk will not interact with the debris swarm at all.

When a large impact fragment is on a close-in orbit that extends into the satellite zone but not beyond it, collisions with the faster-moving small debris there raise its semimajor axis and lower its eccentricity. After repeated excursions, the object eventually circularizes in the satellite zone. The energy change per orbit, ΔE , is characterized by the acceleration from collisions (Equation (12)) times the path length of the interloper’s excursion into the satellite zone. Picturing a body that has a semimajor axis \tilde{a} near the inner edge of the satellite zone (not deep in the unstable region) and sufficient

eccentricity \tilde{e} to reach the middle of the zone, we estimate

$$\Delta E \sim + \frac{\pi \tilde{v}_{\text{rel}}^2}{4 \tilde{\rho} \tilde{r}} \frac{(\tilde{a} + a) \Sigma}{4 a t_{\text{eff}}}, \quad (17)$$

since collisions within the stream of small particles boost the larger body's speed, providing the torque needed to circularize it.

The timescale for boosting the object from a low- \tilde{a} , high- \tilde{e} orbit interior to the satellite zone to a circular orbit in the zone is

$$\begin{aligned} t_{\text{boost}} &= \frac{\tilde{a}}{d\tilde{a}/dt} \approx 4 \frac{\tilde{\rho} \tilde{r}}{\Sigma} \frac{a^2 t_{\text{eff}} (1 + \tilde{e}/2)}{\sqrt{GM} \tilde{a}^{3/2}} \\ &\approx 5.3 \times \left[\frac{1 + \tilde{e}/2}{1.25} \right] \left[\frac{\tilde{\rho}}{1 \text{ g cm}^{-3}} \right] \left[\frac{\tilde{r}}{10 \text{ m}} \right] \\ &\quad \times \left[\frac{\Sigma}{1 \text{ g cm}^{-2}} \right]^{-1} \left[\frac{\tilde{a}}{30 R_{\text{P}}} \right]^{-1/2} \left[\frac{a}{50 R_{\text{P}}} \right]^2 \left[\frac{t_{\text{eff}}}{5^\circ} \right] \text{ yr.} \end{aligned} \quad (18)$$

This estimate illustrates that mass can also move from the unstable region into the satellite zone.

Unless the mass in the debris is significantly larger than the present-day satellite-zone mass, the maximum size of particles trapped in this way is ~ 10 m. This value is disappointingly small if we hope for kilometer-size seeds or ready-made satellites the size of Styx or Kerberos. Furthermore, because of the geometry of the disk, trapping is efficient only for the fraction of 10 m particles with low inclination. Still, the impact debris is generally launched from Charon with an effective inclination of $\sim 25^\circ$, such that a substantial fraction these larger bodies has an inclination that is low enough to interact with the debris swarm within the satellite zone (Figure 3).

In addition to orbital damping, larger fragments can also be ground down by cratering collisions with the swarm of smaller particles. If a large body plunges through the satellite zone from well outside it on an eccentric, low-inclination orbit, ($t \sim t_{\text{eff}}$), it collides with many smaller particles, eroding its surface. As seen in laboratory experiments (Housen & Holsapple 2011, Figure 16 therein) and simulations (e.g., Svetsov 2011), each high-speed collision ($v_{\text{rel}} \sim v_{\text{K}}$) can eject much more than the mass of the small impactor. If we assume that a debris particle removes at least its own mass from the fragment after each collision, then the fragment's fractional mass loss per orbit is

$$\begin{aligned} \frac{\Delta \tilde{m}}{\tilde{m}} &\gtrsim \frac{3}{2 \tilde{\rho} \tilde{r}} \frac{\Delta a \Sigma}{a t_{\text{eff}}} \sim 0.011 \left[\frac{\tilde{\rho}}{1 \text{ g cm}^{-3}} \right]^{-1} \\ &\quad \times \left[\frac{\tilde{r}}{10 \text{ m}} \right]^{-1} \left[\frac{\Delta a}{33 R_{\text{P}}} \right] \left[\frac{\Sigma}{1 \text{ g cm}^{-2}} \right] \left[\frac{a}{50 R_{\text{P}}} \right]^{-1} \left[\frac{t_{\text{eff}}}{5^\circ} \right]^{-1}, \end{aligned} \quad (19)$$

where \tilde{m} is the mass of the large body, and we use its geometric cross section to derive the debris mass that it encounters. From the rightmost expression, it is clear that a 10 m fragment on an eccentric orbit with a semimajor axis of $100 R_{\text{P}}$ loses almost 5% of its mass per year. Smaller particles lose mass at even higher rates.

While a small fragment loses a greater fraction of its mass to erosion than a large fragment, the larger body loses more mass in absolute terms. From Equation (19), a kilometer-size body, with mass 4×10^{15} g, loses 5×10^{11} g per orbit, a thousand times more than a 10 m interloper. Still, as a way to add mass to the satellite zone, the demographics favor the smaller bodies: The number of erosive collisions involving 10 m objects is much larger than for 1 km bodies, and the amount of mass delivered by the smaller bodies is greater as well. If there were as much mass in 10 m objects passing through the satellite zone as there were small debris in the disk, then the disk mass would increase by 25% in five years, depending on the typical inclination of the interloping bodies. Smaller interlopers would contribute even more.

3.6. Summary

From this analysis, we conclude that ejecta from a major impact on Charon can be trapped within the satellite zone. Our main results are (i) the delivery of material to the satellite zone for the formation of the satellites requires a TNO impact with Charon, and (ii) the impact ejecta must consist of debris particles with radii of less than about 10 m to orbitally damp to form a circumbinary disk in the satellite zone. If the material strength of the debris is not strong enough to prevent shattering, a collisional cascade is triggered, yielding a dynamically cool circumbinary disk composed of particles no larger than a few centimeters in radius. In contrast, objects larger than 10 m are likely lost to accretion or ejection by the Pluto–Charon binary.

Collisional damping is at the heart of these impact scenarios. The success of any model requires robust collisional damping to produce a reservoir of circumbinary mass for the satellites. Only debris that can participate in this damping is relevant. All else is lost.

When the evolution of debris from a direct TNO impact on Charon is driven by collisions, the delivery of material to the satellite zone is not efficient. Only about 10% of the high-speed ejecta dynamically settles in the satellite zone. Higher efficiency may be achieved in other scenarios, such as when the debris is entirely composed of micron-size grains that behave like a viscous medium, or if there were a transient gas cloud to aerodynamically trap small debris particles. Another possibility is if a surface-skimming impact concentrates material on orbits that fortuitously lie in the plane of the binary with semimajor axes within the satellite zone. Our simple model of debris from a direct hit on Charon nonetheless provides a baseline for the successful delivery of the building blocks for the satellites from a TNO impact.

4. A Full Demonstration with the ORCHESTRA Code

4.1. Initial Conditions

To explore this model in more detail, we perform several calculations with the full *Orchestra* code. In the multiannulus coagulation routine, an area between $19 R_{\text{P}}$ and $135 R_{\text{P}}$ contains 28 concentric annuli distributed in equal intervals of $a^{1/2}$. Each annulus has 80 mass bins with minimum radius $r_{\text{min}} = 0.01 \mu\text{m}$ and maximum radius $r_{\text{max}} = 1$ m. We seed this grid with solids having total mass $M_0 = 10^{20}$ g, material density 1.5 g cm^{-3} , surface density $\Sigma \propto a^{-2}$, and a size distribution $n(r) \propto r^{-3.5}$. With these initial conditions, most of the mass lies in the largest objects; annuli in the inner portion of the grid have roughly twice the total mass each annulus in the outer portion.

For the eccentricity and inclination of the solids, we consider three sets of initial conditions that span likely outcomes for material ejected from a collision between a KBO and either Charon or Pluto. Solids lie within a thick disk with opening angle $i_0 = 15^\circ$; the initial vertical velocity ranges from $v_z \approx 35 \text{ m s}^{-1}$ at the inner edge of the disk to $v_z \approx 14 \text{ m s}^{-1}$ at the outer edge of the disk. For the initial eccentricity e_0 , we assume orbits with pericenters (a) near the orbit of Charon ($q_a = 15 R_p$; $e_0 = 0.25$ at $20 R_p$ and $e_0 = 0.89$ at $135 R_p$), (b) midway between the orbits of Charon and Pluto ($q_b = 10 R_p$, $e_0 = 0.5$ at $20 R_p$ and $e_0 = 0.925$ at $135 R_p$), and (c) near the orbit of Pluto ($q_c = 2 R_p$; $e_0 = 0.9$ at $20 R_p$ and $e_0 = 0.985$ at $135 R_p$).

To allow the e and i of mass bins to react to the gravity of Pluto and Charon, we assign massless tracer particles to each mass bin. Within an annulus, each mass bin is allocated 160 tracers (12800 tracers for 80 mass bins). Another 3200 tracers are assigned to bins with the most mass per bin. The number (mass) of particles assigned to each tracer is based on the total number (mass) of particles in a mass bin divided by the number of tracers assigned to that bin. In mass bins with few particles, the algorithm assigns integer numbers of particles to each tracer. Thus, some tracers may “carry” more mass than other tracers. Orbital e_0 and i_0 for each tracer follow the e_0 and i_0 for the assigned mass bin. Tracers initially have random orbital phases; some tracers are initially near orbital pericenter, while others are near apocenter. Although the midplane of the disk lies in the Pluto–Charon orbital plane, some tracers initially lie within the orbital plane while others begin their evolution out of the orbital plane. Once assigned to a mass bin, a tracer may move to another annulus in response to gravitational interactions with Pluto, Charon, and the mass in the coagulation grid, but it may not move among mass bins.

In these examples, we do not assign tracers to mass bins with no mass initially. As the calculation proceeds, catastrophic disruption and cratering remove mass from the higher mass bins; fragments of these collisions are placed in lower mass bins. Thus, the largest objects do not grow from mergers; higher mass bins remain empty for the duration of the calculation. In future studies, we plan to investigate the growth of particles that remain in the grid once the damping of relative velocities allows collisions to create larger merged objects.

4.2. Computational Approach

From this initial setup, calculations proceed as follows. With a time step of length Δt , the coagulation code derives the changes in the number, total mass, e , and i of each mass bin from collisions and orbital interactions with all other mass bins. Collision rates are derived from the particle-in-a-box algorithm (e.g., Kenyon & Bromley 2002, 2004a, 2008). For each mass bin k in annulus i , the rate of collisions with solids in mass bin l in annulus j is a function of the number density of particles (n_{ik} and n_{jl}), the collision cross section, the relative velocity, and the overlap of orbits (see Section 2 of Kenyon & Bromley 2008). When $i = j$, the overlap is 1; otherwise, the overlap is approximately the ratio of the volume of annulus j that lies within the volume of annulus i .

For the initial particle velocities considered here, all collisions are destructive, with outcomes set by the ratio of the center-of-mass collision energy Q_c to Q_D^* . The mass ejected in a collision is $m_e = (m_1 + m_2)(Q_c/Q_D^*)$, where m_1 and m_2 are the masses of the colliding planetesimals. Within the ejecta, the largest object has a mass $m_l = m_e(Q_D^*/Q_c)^{b_l}$, where $b_l = 1$.

Smaller fragments follow a power-law size distribution, $n(r) \propto r^{-q}$ with $q = 3.5$. Other choices for b_l and q have little impact on the evolution (Kenyon & Bromley 2016, 2017). With no large objects in the grid, collisional damping dominates dynamical friction and viscous stirring. The Fokker–Planck algorithm within *Orchestra* solves for the damping of each mass bin (Ohtsuki 1992; Ohtsuki et al. 2002; Kenyon & Bromley 2008).

At the end of the coagulation step, each tracer is assigned a target eccentricity e_t and inclination i_t based on its current e_i and i_i and the change in e and i for its mass bin from the coagulation calculation. These targets result in time derivatives for e and i , $de/dt = (e_t - e_i)/\Delta t$ and $di/dt = (i_t - i_i)/\Delta t$. Before the n -body step, tracers are also assigned new numbers and masses of particles based on the number and mass within each mass bin. Although the n -body code does not use this information, each tracer carries a changing mass of solids based on the evolution of solids in the coagulation grid.

Within the n -body step, algorithms update the positions and velocities of tracers and Pluto–Charon. Tracers evolve with their derived de/dt and di/dt and respond to gravitational interactions with Pluto and Charon. The orbits are evolved with a sixth-order symplectic integrator with 200 steps per binary orbit. The tracers’ eccentricity e and inclination i are shifted incrementally over time steps set by the coagulation code, with shift rates determined according to the damping and stirring inferred from the coagulation calculations. These changes to e and i are implemented by small adjustments to the direction of travel and (if necessary) incremental shifts in position, but without affecting the other osculating orbital elements.

At the end of the n -body step, tracers have new positions, velocities, and orbital elements a , e , and i . Tracers with new a substantially different from the “old” a are placed in new annuli. When a tracer lands in a new annulus, the number and mass of particles assigned to that tracer move out of the mass bin in the old annulus and into a mass bin within the new annulus. Some tracers collide with Pluto or Charon; others are ejected beyond the outer limits of the n -body calculation space, $a \gtrsim 1000 R_p$. After these tracers are deactivated for the remainder of the calculation, the coagulation particles associated with these tracers are removed from the coagulation grid. When an active tracer has a semimajor axis outside of the coagulation grid, its mass is removed from the old annulus and is not placed in a new annulus. If that tracer returns to the grid before a collision with Pluto–Charon or ejection, the mass that it carries also returns to the grid.

Although assigning tracers to annuli based on their current position (x , y , z) seems reasonable, placement based on a is more in the spirit of the coagulation code. The collision and Fokker–Planck algorithms derive rates based on particle volumes, $V = 4\pi a \Delta a H$, where $\Delta a \approx \delta a + ea$ and δa is the physical width of the annulus (Kenyon & Bromley 2008). In this application, the physical extent of particle orbits is much larger than the physical width of each annulus. Thus, placing tracers in annuli according to a recovers the correct volume for calculations of collision and stirring rates.

The new orbital elements for tracers inform the e and i of mass bins in the coagulation code. Within each mass bin, we derive the median e and i and their interquartile ranges for the set of tracers assigned to that mass bin. These medians set the new e and i for the mass bin. The interquartile ranges allow us to monitor the accuracy of the median in measuring the typical

e and ι for a set of tracers. Typically, the interquartile ranges are small.

This set of steps provides a closed-loop algorithm that allows the mass bins and the tracers to respond to the gravity of Pluto–Charon and the orbiting solids. The coagulation particles tell the tracers how to react to solid material orbiting Pluto–Charon. In turn, the tracers tell the solid material how to react to Pluto–Charon. As long as time steps are not too long, the lag between the coagulation and n -body steps does not introduce significant offsets in the evolution of the mass bins and the tracer particles. Aside from setting the length of time steps based on the changing properties of the mass bins and the accuracy of the n -body integrator, the code has several constraints to make sure that changes in the evolution of tracer orbital elements within the n -body code are well-matched to changes in the evolution of the mass bins.

Although this algorithm follows the evolution of e and ι well, it does not include a mechanism to transfer tracers from one annulus to another due to a catastrophic collision. In the coagulation code, collision of particles in annulus i in another annulus j results in debris deposited in an intermediate annulus that allows conservation of angular momentum, $j' \approx (i + j)/2$. Formally, we could derive a da/dt to be applied to tracers in the n -body code that would transport the appropriate tracers to the “correct” semimajor axis. However, this approach is computationally expensive. For the present study, we allow the coagulation code to transfer material from one annulus to another through cratering collisions and catastrophic disruptions. Active tracers in annuli that receive additional material from collisional evolution are assigned more or less mass every time step based on the changing contents of mass bins in the coagulation code.

4.3. Results

The evolution of the orbiting solids in calculations with different q ($q_a, q_b, q_c = 15, 10, 2 R_p$) all follow a similar path. Prograde orbits with $a \lesssim 1.7 a_{PC}$ are unstable (Kenyon & Bromley 2019b). Despite short collisional damping timescales for solids with $a \approx 18\text{--}30 R_p$, the central binary gradually clears away tracers and their associated solids in this semimajor axis range on one year timescales. Before this clearing is complete, destructive collisions between particles in the innermost annuli and other mass bins deposit debris in other annuli. This process effectively transports some material from inside the unstable region to annuli outside the unstable region. As tracers in the inner disk are damped and cleared, some move onto orbits with larger a (due to dynamical interactions with Pluto–Charon) but lower e and ι (due to damping). Over time, these tracers and their associated solids may remain on stable orbits in the outer part of the disk.

At large distances, $a \approx 100\text{--}135 R_p$, collision timescales are 40–50 times longer than timescales at $30\text{--}40 R_p$. Solids in this semimajor axis range have $e \approx 0.9$ and damp slowly. Although collisions deposit debris into the inner disk, transport of material from the outer disk inward is much slower than transport from the inner disk outward. As this material evolves, tracers on high e orbits often interact with Charon. The slow progress of collisional damping prevents these tracers from evolving to smaller e before they suffer a large impulsive encounter with Charon. Over time, the central binary ejects nearly all of this material.

At intermediate distances from the central binary, $a \approx 30\text{--}100 R_p$, the fate of solids depends on the initial eccentricity. In systems with $q \approx q_c - q_b$, collisional damping needs to raise the pericenter to $q \gtrsim 25 R_p$ to avoid strong dynamical encounters with the central binary. Although damping raises q , this evolution is slow compared to the loss of material from dynamical encounters with Pluto or Charon. In model (b), it takes 1 yr (10 yr) to remove 93% (98%) of the solids. Model (c) evolves faster: it takes less than a day (month) to lose more than 90% (99%) of the solids. After 100 yr, both models settle into a steady state, where the mass changes very slowly with time. At this point, model (b) (model (c)) has 2% (0.006%) of its initial mass remaining in orbit around Pluto–Charon.

When $q \approx q_a$, collisional damping works fast enough to raise the pericenter of all of the solids on typical dynamical timescales. Although the central binary evacuates the region with $a \approx 18\text{--}30 R_p$ in ~ 1 yr, some tracers and their associated solids are placed on lower e orbits with $a \gtrsim 30 R_p$. Collisional damping continues to lower e for these tracers; they remain on fairly stable orbits on $10\text{--}100$ yr timescales. At $100\text{--}135 R_p$, collisional damping is fast enough to slow the loss of material compared to the model (b) and (c) calculations. On 100 yr timescales, however, much of this material is still lost.

For systems with $q \approx q_a$, collisional damping enables retention of a significant fraction of solids at $a \approx 30\text{--}100 R_p$. After one month (year), the system has 88% (78%) of its initial mass. Although the loss of material reaches $\sim 35\%$ (38%) after 10 yr (100 yr), subsequent losses are small. Most of this material has $a \approx 45\text{--}75 R_p$, which overlaps the satellite zone at $33\text{--}66 R_p$.

Figure 5 illustrates the time evolution of Σ in all three models. In each panel, the thin black line plots the initial surface density distribution, $\Sigma \propto a^{-2}$. The points indicate the surface density in each annulus at the time (in yr) indicated in the upper right corner of each panel for models with $q = q_a$ (blue points), $q = q_b$ (green points), and $q = q_c$ (orange points). The rapid evolution in the inner and outer disk is apparent: it takes only 5–10 days to begin to remove solids at $20\text{--}30 R_p$ and at $110\text{--}135 R_p$. In between these limits, collisional damping tries to drive the solids to lower e and lower ι before tracers are ejected or collide with Pluto or Charon. For the model (b) and (c) parameters, collisional damping is too slow at $30\text{--}100 R_p$. Although material is lost more slowly than solids in the inner or outer disk, the reduction in surface density is steady at all a .

In the $q = q_a$ calculation, the evolution concentrates solids in annuli at $50\text{--}70 R_p$. As with the other calculations, the central binary steadily removes material in the inner disk and the outer disk. The timescale for this evolution is 1–10 yr. At $t = 1$ yr (Figure 5, middle right panel), the surface density at $50\text{--}80 R_p$ is larger than the initial Σ . After another 9 yr, the region of large Σ is smaller; however, the region at $50\text{--}75 R_p$ still has a surface density somewhat larger the starting point. After 100 yr (Figure 5, lower right panel), the surface density at $\sim 55\text{--}80 R_p$ is at least as large as the initial surface density.

When $q = q_a$ and $t = 30\text{--}200$ yr, the surface density at $50\text{--}80 R_p$ oscillates slowly with time as tracers on modest e orbits move into and out of the coagulation grid. Overall, the total mass within the coagulation grid is fairly constant, varying by roughly a few percent from one time step to the next. Throughout this period, the typical e and ι of tracers gradually declines. At $100\text{--}200$ yr, particles with $a \approx 50\text{--}80 R_p$ have

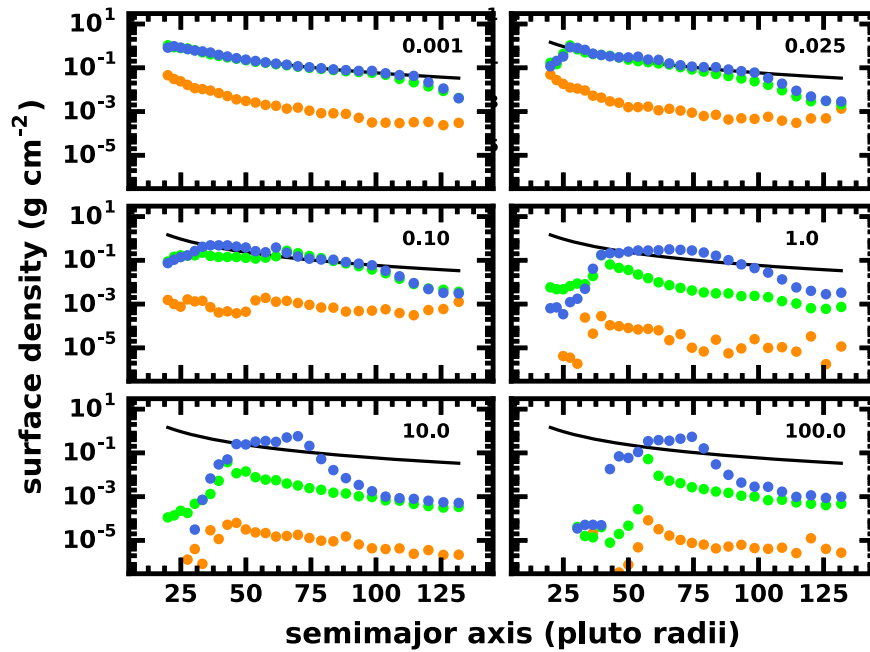


Figure 5. Time evolution of the surface density in rings of solids at 19–135 R_p for systems with $q = q_a$ (blue points), $q = q_b$ (green points), and $q = q_c$ (orange points). Solid black line in each panel indicates initial surface density. Evolution time (in yr) is in the upper right corner of each panel. Systems with $q \approx q_b - q_c$ lose nearly all of their solid material in 10–100 yr. Systems with $q = q_a$ generate into a dense ring of solids at 50–80 R_p in 10–100 yr; the cm- to m-sized solids then begin to grow into larger objects.

typical $e \approx 0.01$ and $\iota \approx 10^{-4}$. This part of the swarm is vertically thin and free from large dynamical interactions with Pluto–Charon.

Once the solids settle down into low- e , low- ι orbits at 100–200 yr, mergers start to dominate collision outcomes. Typical center-of-mass collision energies, $Q_c \approx 2\text{--}3 \times 10^4 \text{ erg g}^{-1}$, are smaller than typical binding energies, $Q_D^* \approx 5\text{--}10 \times 10^5 \text{ erg g}^{-1}$. For computational simplicity, we do not place tracers in mass bins with $r \gtrsim 1 \text{ m}$, preventing *Orchestra* from following the growth of the largest objects. We therefore terminate the calculation. Based on previous results (Kenyon & Bromley 2014), we expect the swarm of 1 cm–1 m objects to grow into a few 1 km satellites in 100–1000 yr. Once satellites reach these sizes, subsequent growth is chaotic; likely outcomes include 5–20 km satellites with masses similar to the known moons in the satellite zone.

To place the evolution of Figure 5 in the context of other giant impact calculations, we examine the evolution of Σ , e , and ι as functions of the “radius of the equivalent circular orbit” (e.g., Canup 2004, 2011; Nakajima & Stevenson 2014)

$$a_{\text{eq}} = a(1 - e^2). \quad (20)$$

For each tracer, the angular momentum is $L^2 = G(m_p + m_c)a(1 - e^2)$; thus, a_{eq} provides a way to track the angular momentum evolution of the swarm.

At the start of each calculation, all of the solids have a pericenter near Charon (the $q = q_a$ model), near Pluto (the $q = q_c$ model), or in between (the $q = q_b$ model). With $a_{\text{eq}} = q(1 - e)$ and $e > 0$, the initial a_{eq} lies inside q . As the calculations proceed, collisional damping gradually reduces e for many solids; in turn, a_{eq} slowly increases. Throughout the evolution, the central binary ejects other solids from the system. Although the a_{eq} for this material also increases with time, these solids have $e \gtrsim 1$ and a range of ι . For short periods

of time, unbound material contributes to the surface density for all $a_{\text{eq}} \gtrsim 0$.

In the $q = q_c$ model, competition between collisional damping and dynamical ejections generates two distinct sets of solids in the (a_{eq}, e) plane (Figure 6). At $t = 0$, all points lie on a nearly vertical line at $a_{\text{eq}} \approx 0$ between $e \approx 0.9$ and $e \approx 0.99$. In a few hours, collisional damping creates the swath of points with $a_{\text{eq}} \approx 5\text{--}20 R_p$ and $e \lesssim 0.9$ (Figure 6, upper left panel). At the same time, the central binary ejects solids along a locus with $e \approx 1$ and $a_{\text{eq}} \approx 10\text{--}200 R_p$. Although this rapid evolution is striking, the dynamical parameters of most tracers remain unchanged; these tracers lie in the magenta clump in the upper left corner of this panel.

Over the next year, collisional damping drives a swarm of tracers into the midplane of the central binary. After ~ 10 days, a dense knot of tracers lies within a narrow ring at $a_{\text{eq}} \approx 20 R_p$ (approximately the semimajor axis of Charon). Most of this material has $e \lesssim 0.1$; some with larger e approaches the ring from smaller a_{eq} (Figure 6, upper right panel). This ring expands to $a_{\text{eq}} \approx 30 R_p$ at $t = 0.1 \text{ yr}$ (Figure 6, middle left panel), and then into a disk close to the satellite zone at $a_{\text{eq}} = 40\text{--}80 R_p$ after a year of evolution (Figure 6, middle right panel).

Throughout this period of disk formation, collisional damping drives material from orbits with small a_{eq} and large e to those with larger a_{eq} and smaller e . This evolution generates a slanted line of points in the figure. At early times, this line appears to feed the dense ring at small a_{eq} . At later times, this line feeds the forming disk outside the dense ring. Eventually, there are no tracers in the region between the disk and the set of tracers on unbound orbits (Figure 6, lower panels). Although we halted the evolution after 100 yr, some of the tracers above the disk in the lower panels will join the disk at large a_{eq} .

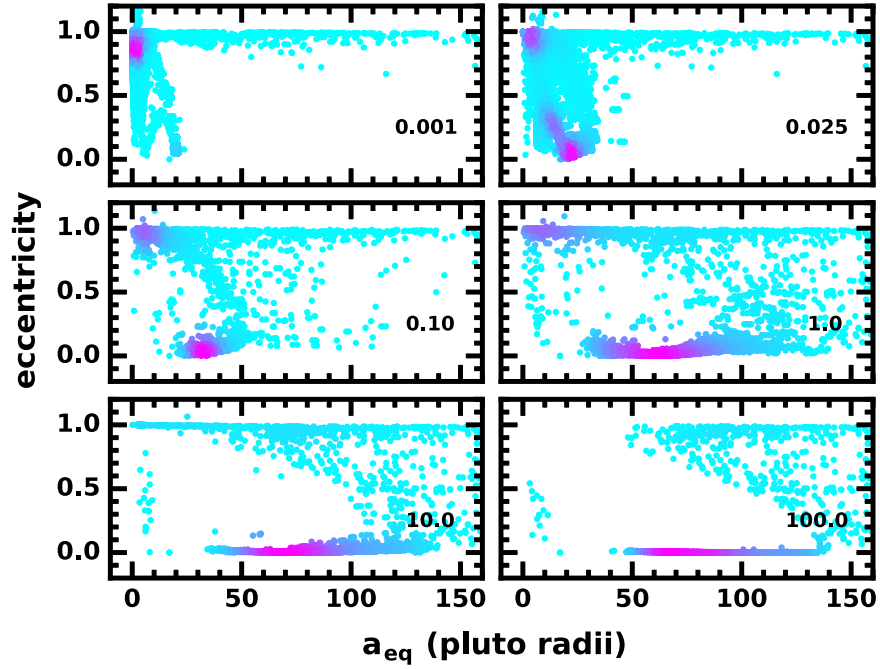


Figure 6. Time evolution of solids in the (a_{eq}, e) plane for the $q = q_c$ model. Cyan points indicate the positions of individual tracers. Magenta points denote regions of high density; the intensity of the color provides a measure of the density. The evolution time in years is listed in the lower right corner of each panel.

As many tracers join the disk, the central binary ejects others. These tracers form a line with $e = 1$ and all $a_{\text{eq}} \gtrsim 0$. The actions of collisional damping and dynamical ejections gradually deplete the knot of tracers at $(a_{\text{eq}}, e) = (0, 1)$ in Figure 6. After $t \approx 10$ yr (100 yr), there are few (no) tracers in this knot. Another few hundred years of evolution will probably eliminate all tracers with $e \approx 1$ from the diagram.

Figure 7 repeats Figure 6 for the inclination of particles in the $q = q_c$ model. At $t = 0$, all tracers have $a_{\text{eq}} \approx 0$ and $i \approx 0.25$. Within a few hours, ejections from the central binary establish a set of tracers with small a_{eq} and large i (Figure 7, upper left panel). Another set of ejected particles has $a_{\text{eq}} > 0$ and $i \approx 0.25$. A third group has damped into the orbital plane ($i \approx 0$). As with e , there is a set of tracers along a line from the dense knot at $(a_{\text{eq}}, i) = (0., 0.25)$ to the midplane.

As the evolution proceeds, tracers continue to be ejected along lines with $a_{\text{eq}} \approx 0$ or $i \approx 0.25$. Several tracers not shown in the figure are ejected on retrograde orbits relative to the central binary. From $t = 0.001$ yr to $t = 1$ yr, more and more tracers are ejected along the line with $i \approx 0.25$ compared to the line with $a_{\text{eq}} \approx 0$. At $t = 10$ – 100 yr, tracers remaining to be ejected have $a_{\text{eq}} \gtrsim 50$ – $100 R_p$ and $i \approx 0.25$. After another few hundred yr, the central binary will eject these tracers.

As most tracers disappear from the system, collisional damping drives a second set of tracers into the midplane. At early times (Figure 7, upper right panel), tracers from the initial knot feed into the growing ring at $a_{\text{eq}} \approx 20 R_p$. Expansion of this ring into a disk accompanies the depletion of the initial dense knot of tracers (Figure 7, middle panels). After most tracers have been ejected, a dense disk of tracers remains in the midplane of the binary (Figure 7, lower panels). Much of this disk lies within the satellite zone.

The evolution of tracers in the $q = q_b$ model follows the evolution in Figures 6–7. Having somewhat smaller (larger) e (q), these tracers initially form a dense knot in (a_{eq}, e) space at somewhat larger (smaller) a_{eq} (e). Collisional damping and

dynamical ejections then transform this knot into a dense disk of solids in the midplane of the binary and a swarm of material flowing out of the system. Although some material is ejected at large i with respect to the midplane, most flows out through a disk-shaped volume with its equator in the binary midplane and an opening angle of $i \approx 0.25$. Compared to the $q = q_c$ model, more material remains in the disk and ejections are less frequent.

When $q = q_a$, the evolution of tracer parameters as a function of a_{eq} changes dramatically (Figure 8). In this model, material initially has a broad range of eccentricity, $e \approx 0.25$ – 0.9 . In the (a_{eq}, e) plane, tracers occupy a line extending from $(a_{\text{eq}}, e) = (20, 0.25)$ to $(a_{\text{eq}}, e) \approx (0, 0.9)$. Within a few hours, damping places some tracers within a narrow ring at $a_{\text{eq}} \approx 20 R_p$ in the midplane of the binary. The central binary ejects others into a swath with $a_{\text{eq}} \approx 20$ – $50 R_p$ and $e \approx 0.3$ – 0.7 (Figure 8, upper left panel).

At later times, damping and dynamical ejections continue to evolve tracers along different paths. After 0.025 yr, there is a dense concentration of solids in a broad ring with $a_{\text{eq}} \approx 20$ – $30 R_p$ (Figure 8, upper right panel). Damping also translates an ensemble of tracers from their initial $(a_{\text{eq}}, e) \approx (20, 0.25)$ to $(25, 0.25)$. In contrast, interactions with the central binary displace another set of tracers toward larger a_{eq} and larger e : there is a dense clump of tracers at $(a_{\text{eq}}, e) = (40, 0.5)$ in the midst of a large group on its way out of the system.

During the next 0.1–1 yr, these two groups of solids diverge more and more dramatically in the (a_{eq}, e) plane (Figure 8, middle panels). The dense clump of tracers at $(a_{\text{eq}}, e) = (20, 0.25)$ vanishes. The dense clump in the midplane grows in mass and expands to $a_{\text{eq}} \approx 40 R_p$. Although several tracers remain behind at small a_{eq} , most of the remaining tracers move to larger a_{eq} at ever-increasing e .

By 10–100 yr, disk formation within the satellite zone is nearly complete (Figure 8, lower panels). Although the disk extends from $30 R_p$ to beyond $150 R_p$, the densest concentration of

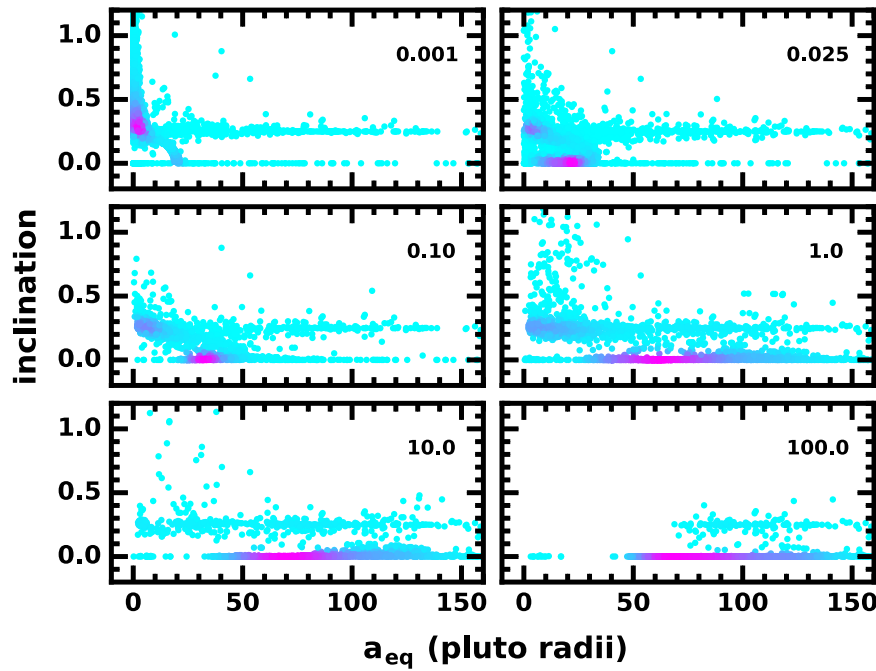


Figure 7. As in Figure 6, for the inclination.

tracers at 55–75 R_p overlaps the satellite zone. Aside from several dozen tracers at small a_{eq} and small e , few tracers have orbits with $a_{eq} \lesssim 50$ –70 R_p and $e \gtrsim 0.05$. At larger a_{eq} , tracers are either within the disk, damping into the disk at $a_{eq} \gtrsim 150$ R_p , or leaving the system on high- e orbits.

Figure 9 illustrates the time evolution of tracers in the (a_{eq}, i) plane when $q = q_a$. Starting from a configuration where solids lie in a horizontal line with $a_{eq} = 0$ –20 and $i = 0.25$, the central binary ejects a few tracers along retrograde orbits and pushes a much larger subset of tracers into high inclination orbits (Figure 9, upper left panel).

Collisional damping drives another large group into a low-density ring in the orbital plane of the central binary. After only 9–10 days (Figure 9, upper right panel), many tracers have low-inclination orbits ($i \approx 0$) extending from $a_{eq} \sim 0$ to $a_{eq} \gtrsim 150$ R_p . The density of tracers in the narrow ring at $a_{eq} \approx 20$ –35 R_p is then larger than the density in the original knot at $(a_{eq}, i) = (20, 0.25)$ or the ensemble of tracers ejected on high-eccentricity orbits with large a_{eq} and $i \approx 0.25$.

As the calculation proceeds, tracers separate into two distinct groups. In the orbital plane of the binary, the position of the narrow ring moves from $a_{eq} \approx 20$ R_p to $a_{eq} \approx 40$ R_p in 1 yr (Figure 9, middle panels). At later times, the ring expands into a disk which extends from 30 R_p to $\gtrsim 100$ R_p . The densest part of this ring lies within the satellite zone (Figure 8, lower panels).

As the disk forms, the central binary ejects tracers in all directions. Although some tracers pass out of the system on high-inclination orbits, most follow lower-inclination trajectories with $i \lesssim 0.25$. During the first 0.1–1 yr, the binary evacuates inner regions with $a \lesssim 30$ R_p . Tracers at larger a on longer-period orbits encounter the binary less frequently and are ejected on longer timescales of 10–100 yr. After 100 yr, there are only a few tracers with $a_{eq} \lesssim 70$ R_p . High-inclination tracers at larger a_{eq} will be ejected over the next few hundred years.

The evolution outlined in Figures 6–9 illustrates the transformation of a high-eccentricity, high-inclination swarm of solids into a vertically thin disk that overlaps the satellite zone. To show how the surface density evolves, we assign tracers to discrete bins in a_{eq} , sum the mass carried by each tracer, and divide by the area for each bin. Figure 10 shows snapshots of the surface density distribution $\Sigma(a_{eq})$ for the same epochs shown in Figure 5. At the start of each sequence, $a_{eq} \approx q$; all of the solids are bunched up close to Charon. In the $q = q_a$ model (Figure 10, blue points), 0.001 yr of collisional damping generates a ring with high surface density at 20–50 R_p and an extended region with low surface density at 50–150 R_p . Over 10–100 yr, the dense ring expands outward, reaching 45–75 R_p . Inside this ring, the surface density drops by a factor of 100–1000. Outside, Σ grows by a factor of 100.

Although collisional damping tries to generate a dense ring in the other models, dynamical ejections are more efficient. In the $q = q_c$ model (Figure 10, orange points), some material lies within the low- Σ extended region. Over time, the surface density in this model gradually declines. In the $q = q_b$ model, a small dense ring is well-defined at 0.001–0.1 yr. However, the surface density slowly declines with time, leaving behind an extended disk with low surface density at 50–150 R_p .

4.4. Outcomes

Outside the dense ring of solids at 50–80 R_p , the evolution has several likely outcomes. Inside 35–40 R_p , where the surface density is low, the eccentricity is small $e \approx 0.01$ –0.02. With low e and little mass, these solids will either remain in their present state or collide with material at somewhat larger distances. Either way, satellite formation at 30–40 R_p is unlikely. Beyond 80–90 R_p , roughly half of the mass is in small (large) solids with $r \lesssim 3$ –5 cm ($r \gtrsim 5$ –10 cm) and $e \lesssim 0.01$ ($e \gtrsim 0.1$). With such a small surface density, collisions are rare; damping is slow. Although safe from interactions with Charon, these solids are unlikely to merge into larger objects but may merge with solids in the dense ring. Collectively, the

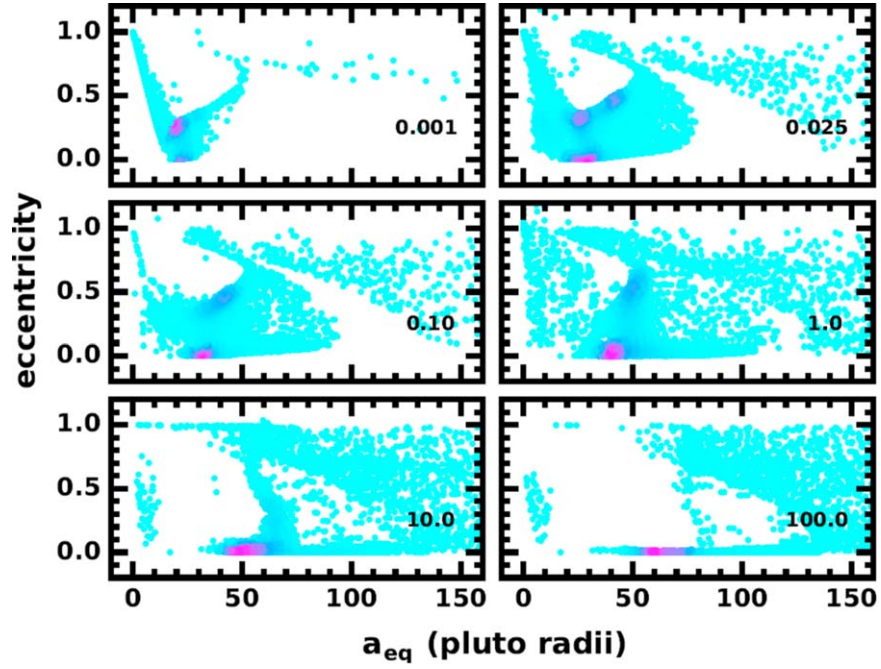
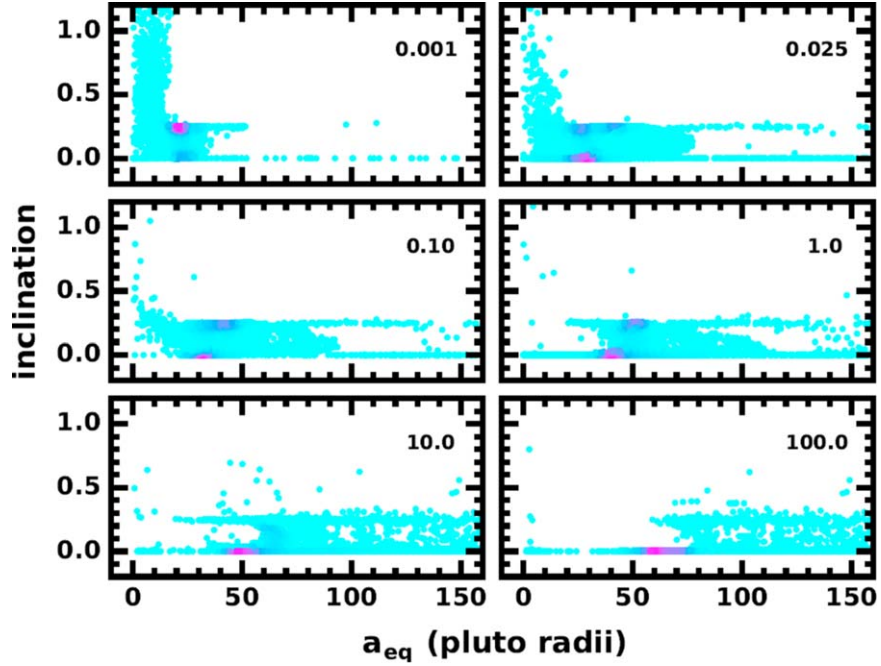
Figure 8. As in Figure 6, for the $q = q_a$ model.

Figure 9. As in Figure 8, for the inclination.

solids at $30\text{--}40 R_p$ and at $90\text{--}130 R_p$ have a total mass comparable to the mass of Styx, $m \approx 7 \times 10^{17}$ g. With such little mass, this material will have little impact on the formation of satellites in the dense ring.

Once growth is complete at $50\text{--}80 R_p$, the low-density material at $30\text{--}40 R_p$ and at $90\text{--}130 R_p$ may play a role in shaping the final configuration of the satellites. With more material in the outer disk than the inner disk, satellites may migrate inward toward the central binary (Kenyon & Bromley 2014; Bromley & Kenyon 2015). Satellites cannot

migrate into the unstable region inside $30 R_p$ due to the lack of material. However, migration could place small satellites—like Styx—inside the dense ring at $50\text{--}80 R_p$.

Several test calculations suggest the formation of a dense ring in the satellite zone is the inevitable outcome of evolution when material has $q \approx a_c$. Systems with steeper (shallower) surface density gradients allow ring formation somewhat closer (farther) away from the central binary than the ring in Figure 5. In a future study, we plan to consider how outcomes depend on the initial conditions in more detail.

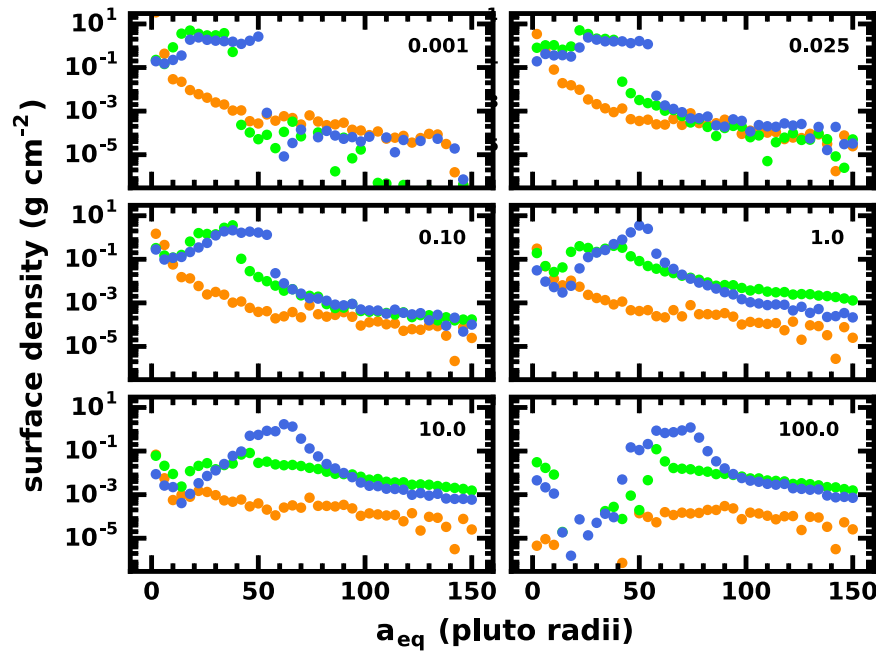


Figure 10. Snapshots of the surface density in calculations with $q = q_a$ (blue points), $q = q_b$ (green points), and $q = q_c$ (orange points) at times (in yr) indicated in the upper right corner of each panel. After 100 yr, the $q = q_a$ model has a dense ring at 50–80 R_p within a lower-density disk at 40–150 R_p . This ring is stable. In the other models, the surface density within the ring and the disk gradually decline with time.

4.5. Summary

Calculations with *Orchestra* demonstrate that the evolution of ejecta from an impact with Pluto or Charon is a competition between collisional damping and removal by the central binary. Unless impact debris is launched from Charon’s orbital distance, less than a few percent of the debris remains after ~ 100 yr. Satellite formation is then unlikely unless the original ejecta mass is significantly larger than $M_{\text{snkh}} \sim 10^{20}$ g. A launch from Charon is much more promising. After ~ 100 yr of collisional evolution, more than 60% of the debris remains in low-eccentricity orbits around the central binary. This material is constrained to a region that is representative of the satellite zone, with little mass outside of it. The resulting satellite system (Kenyon & Bromley 2014) will be truncated, consistent with the absence of moons beyond Hydra.

Natural extensions of these calculations include a consideration of different particle densities, initial size distributions, and orbital configurations, as suggested by the analytical estimates in Section 3.

5. Discussion

The goal of this work is to explore models for creating a reservoir of mass for the small satellites of Pluto and Charon from a Charon–TNO impact. Above (Sections 3 and 4), we consider mechanisms and conditions for settling ejecta from a direct hit on Charon into the satellite zone around the binary. In this section, we discuss these assessments in the broader context of the TNO impact. Our main concerns include how big the impactor must be, given the efficiency of the delivery of impact ejecta to the satellite zone, and the likelihood of such a collision with Charon over the history of the solar system.

As we describe in Section 3, impact debris must orbitally damp quickly in order to settle into the satellite zone before being ejected or accreted by the binary. The efficiency of this process is key to understanding the impact event itself. When

damping is driven by collisions (Section 3.3), dynamical cooling is rapid but only if debris particles are small and numerous enough to support a high collision rate (see Equation (1)). When the TNO impact launches just enough mass into the satellite zone to build the satellites, then the debris particles must be less than about 10 m in radius to settle there through collisional processes. When the debris particles are larger, the ejecta must have a greater total mass for settling to occur. We explore the connection between ejecta and impactor in more detail in Section 5.1.

Gas drag within a cloud of vaporized ice produced in the original impact with Charon offers another possible pathway for delivering debris to the satellite zone (Section 3.4). Small debris particles can become entrained in the gas and settle to the midplane as the cloud evaporates. A cloud with a mass of $0.1M_{\text{snkh}}$ can entrain submillimeter grains; trapping larger grains requires more gas. If the debris initially consists of particles that are too large to be entrained, a collisional cascade may grind the debris into particles of the right size. Depending on how the particle sizes evolve, as well as upon the uncertain details of the gas dynamics, a majority of the small debris may be captured in the gas cloud. This effect could help reduce the amount of ejecta needed to get mass to the satellite zone.

In both scenarios, an impact on Charon generates a reservoir of small particles in a thin, dynamically cold circumbinary disk. These solids are capable of trapping or eroding larger debris fragments. In models where the mass of small debris particles is comparable to the total mass of the Pluto–Charon satellites, the maximum size of particles that can be trapped is about 10 m. Depending on the size distribution and orbital elements of these larger bodies, trapping will further increase the mass available to build Kerberos and the others.

With or without these larger “seed” fragments, coagulation processes lead to the growth of the satellites (e.g., Kenyon & Bromley 2014). This outcome is possible because the debris around Pluto–Charon is well outside the Roche limits of the

central bodies. In contrast, the small particles that make up Saturn’s rings lie within the planet’s Roche limit, where tidal forces prevent them from sticking together. The rings are long-lived for this reason. We conclude that a circumbinary disk produced by a Charon–TNO impact will inevitably form satellites.

5.1. The Mass of the Impactor

To make a Charon-impact scenario plausible, the giant cratering event from the TNO collision must eject enough material to account for the satellites. We estimate the necessary mass with guidance from the simulations in Section 3. The tracer particles in these simulations represent the high-speed impact ejecta capable of escaping Charon’s Hill sphere. Only about 1% of these particles end up in the satellite zone after damping “in place” around their osculation semimajor axis. This result suggests that the mass of the high-speed ejecta may need to be as high as $\sim 100 \times M_{\text{snkh}}$. However, because the number density of particles is high in the satellite zone, bound debris that passes through it can get trapped there (Section 3.5). Then, as many as 10% of the tracers may end up in the satellite zone (Figure 4). In this case, the minimum mass of the high-speed ejected debris is about 10^{21} g, or $10 \times M_{\text{snkh}}$.

The mass of the impactor needed to eject $\sim 10^{21}$ g depends on uncertain characteristics of the impactor’s composition and structure, along with the physics of the collision, including the impactor’s speed and angle of impact. To address the impact geometry, we consider limiting cases. In a direct hit, where the projectile impacts Charon head-on, the impactor is obliterated, launching debris and leaving a giant crater. In a surface-skimming event, where the TNO plows into Charon at an oblique angle, material is ejected along the impactor’s general direction of travel. We assume that the impactor is also destroyed in this case as well, although debris may be launched similarly even if the impactor survives and continues on its way after it scrapes debris from the surface of Charon, as in the “hit-and-run” scenario for the formation of the Pluto–Charon binary itself (Canup 2005).

The direct-hit scenario is likely inefficient, requiring an impactor with substantially more mass than is currently in the satellites. The oblique case may be efficient, involving a lower-mass TNO, if the impact hits Charon from a direction that puts debris on low inclination orbits in the satellite zone. The chance that the impact geometry (impact parameter, direction of travel relative to Charon’s orbit around Pluto) is just right may be low compared with the geometry required of a direct impact, for which the simulations suggest that the location of the impact on the surface of Charon is not a major factor. However, because smaller TNOs are significantly more common than larger ones (see below), the surface-skimming impact scenario may be at least as likely as a direct hit by a larger TNO.

In this preliminary work, we focus on the direct-hit scenario. Our simulations are idealizations of this case, and elegant scaling laws provide quantitative predictions for aspects of cratering events (e.g., Holsapple 1994). One of these laws yields the impactor mass required to eject debris at the speeds needed to populate the satellite zone:

$$\frac{M(v)}{M_{\text{im}}} = C \left(\frac{v}{v_{\text{im}} \cos \theta_{\text{im}}} \right)^{-3\mu} \left(\frac{\rho_{\text{im}}}{\rho_{\text{C}}} \right)^{1-3\nu}, \quad (21)$$

where $M(v)$ is the mass ejected with speed greater than v (Holsapple 1994; Housen & Holsapple 2011). The parameters

M_{im} , v_{im} , and θ_{im} are the impactor’s incoming mass, speed, and incidence angle, respectively. The constant C and index μ depend on properties of the target material; the index ν accounts for the effect of any difference in mass density between target (ρ_{C}) and impactor (ρ_{im}). We caution that the power-law dependence is strictly valid for the case of a small impactor and a planar target. In our case, the mass ratio of projectile and target is expected to be small ($<1\%$), but the ratio of radii ($\sim 10\%$) is not.

To apply Equation (21), we assume that the target, Charon, is “well-baked” by tidal interactions with Pluto and thus has low porosity. Then, the index $\mu = 2/3$, consistent with the velocity distribution in our simulations if tracers represent identical masses (see Shuvalov 2009; Housen & Holsapple 2011; Svetsov 2011). While we usually treat the density at Charon’s surface to be the same as that of the impactor, we set the index $\nu = 0.4$ (Housen & Holsapple 2011). Our choice for the constant C is 0.03, consistent with hydrodynamical simulations of other nonporous material (e.g., Svetsov 2011). We assume an angle of incidence $\theta_{\text{im}} = 0^\circ$ (a head-on collision), and an impact speed of $v_{\text{im}} = 2 \text{ km s}^{-1}$, typical of the relative speed between Plutinos and other TNOs (Dell’Oro et al. 2013). Finally, we set the threshold speed v to be 95% of the surface escape velocity of Charon, as in our tracer simulations.

Putting these values together, the impactor mass is

$$\begin{aligned} M_{\text{im}} &\approx \frac{M(v)}{C} \left(\frac{v}{v_{\text{im}} \cos \theta_{\text{im}}} \right)^{3\mu} \left(\frac{\rho_{\text{im}}}{\rho_{\text{C}}} \right)^{3\nu-1} \\ &\approx 3.1 \times 10^{21} \left[\frac{M(v)}{10 M_{\text{snkh}}} \right] \left[\frac{C}{0.02} \right]^{-1} \\ &\quad \times \left[\frac{v_{\text{im}}}{2 \text{ km s}^{-1}} \right]^2 [\cos \theta_{\text{im}}]^2 \left[\frac{\rho_{\text{im}}}{\rho_{\text{C}}} \right]^{0.2} \text{ g}, \end{aligned} \quad (22)$$

which corresponds to an impactor radius of 100 km for a density of $\rho_{\text{im}} = 1 \text{ g cm}^{-3}$. The efficiency of ejecta production increases with impactor density and collision speed. For example, raising v_{im} to 3 km s^{-1} cuts the impactor mass in Equation (22) by more than a factor of two. An increase of closing speed to 4 km s^{-1} would allow a 60 km impactor to deliver $10 \times M_{\text{snkh}}$ of mass to the satellite zone. Conversely, increasing the incidence angle reduces the efficiency.

Our expectation is that an impact between Charon and an object with mass derived from Equation (22) would produce considerably more debris than the point-mass scaling formalism suggests (see Svetsov 2011; Arakawa et al. 2019). One reason is that ejecta is launched from a convex target, not a planar one. It is plausible that a 100 km impactor could generate at least its own mass in high-speed ejecta. By the same token, the parameters adopted in other work lead to predictions with much less debris for the same impactor mass (e.g., Bierhaus & Dones 2015).

If we have overestimated the debris production of a 100 km impactor, and if only 1% of the high-speed ejecta settles in the satellite zone, then the impactor must be disturbingly large, over 200 km in radius. With a mass well over 10^{22} g, this object could significantly deflect Charon in its orbit around Pluto, possibly initiating a second phase of tidal evolution. For this reason, and because such a high-mass TNO is comparatively rare in the outer

solar system, a low-mass impactor plays a more credible role in the scenarios hypothesized here.

As an alternative to a direct hit by a 100 km TNO, an oblique, surface-skimming impact from a smaller body might also produce enough debris to make the satellites. For example, a 30 km impactor has a disruption threshold Q_D^* of about $5 \times 10^8 \text{ erg g}^{-1}$ (Benz & Asphaug 1999, Figure 5 therein); its specific kinetic energy is $2 \times 10^{10} \text{ erg g}^{-1}$. A surface-skimming impact (an oblique impact with “erosion” in Leinhardt & Stewart (2012)) has the potential to completely break up the impactor and impart enough kinetic energy to launch about ten times its mass from Charon’s crust along its direction of travel. In an event where the ejecta are “beamed,” the impact geometry matters. A bad strike, with an impactor that hits Charon on a path aimed at Pluto, could beam all the debris right into the larger planet. A fortunate strike has a trajectory in the plane of the binary, tangential to Charon’s orbit, and intersecting with Charon at a point opposite from Pluto. Then debris would then be on prograde, low-inclination orbits.

In summary, the production of the Pluto–Charon moons from a direct hit probably requires an impactor that is 10–100 times the mass of the satellites, or 50–100 km in radius, depending on the impact speed. Higher speed, near the tail of the TNO velocity distribution, allows the smaller mass. An even smaller TNO (a radius of 30 km or even less) may be sufficient in a fortuitously aimed surface-skimming event.

5.2. The Size Distribution of the Ejecta

The success of a TNO impact as the origin of the Pluto–Charon satellites depends on having most of the impact ejecta in the form of small particles. Particles with radii less than a centimeter damp rapidly. Larger objects with radii of 1–10 m and total mass of 0.3–1.0 M_{snk} initiate a collisional cascade to produce centimeter-sized objects, which then damp rapidly. In a direct-hit scenario, small sizes for the debris are plausible. From studies of impact fragmentation, nearly all of the mass of debris is in small objects (e.g., Melosh et al. 1992); meter-sized bodies may even be the most prevalent (Melosh 1984). For a surface-skimming impact, the specific kinetic energy exceeds the disruption threshold by two orders of magnitude; as in Benz & Asphaug (1999), for example, we do not expect large fragments from the projectile to survive.

5.3. Likelihood of a Charon-impact Event

A key factor for the viability of our model is the probability that a large TNO has collided with Charon since the formation of the binary. Toward the goal of estimating this likelihood, we define N_{50} as the total number of objects with radius $r > 50$ km in the Kuiper Belt today. From the observed brightness distribution of TNOs, Petit et al. (2011) estimate $N_{50} \approx 10^5$ (see their Table 5). Since the Kuiper Belt was more massive at early times (e.g., Kenyon 2002, and references therein), we introduce a scale factor, $x_{\text{KB}} \geq 1$, giving the ratio of mass in the Kuiper in some past epoch relative to its mass today, roughly $0.01 M_{\oplus}$ (e.g., Fraser et al. 2014; Pitjeva & Pitjev 2018). When the solar system was young, the mass was as high as 1–10 M_{\oplus} (e.g., Kenyon & Luu 1999b; Kenyon 2002; Levison et al. 2008; Booth et al. 2009; Schlichting & Sari 2011; Schlichting et al. 2013; Kenyon & Bromley 2014), implying $x_{\text{KB}} \approx 100$ –1000. Collision probabilities for specific solar system bodies scale the same way. Large impacts on Charon (and

Pluto) were as much as 100–1000 times more frequent 3–4 Gyr ago than they are today.

The rate of collisions between Charon and these large TNOs depends on several factors in addition to their total number, $x_{\text{KB}} N_{50}$. The collision cross sections of Charon and the impactors play a part, along with the orbital characteristics that determine how frequently orbits cross. Formally, the collision rate is

$$\eta \approx N(r, t) P_i \pi (r + R_C)^2 \approx 0.03 x_{\text{KB}} \left[\frac{N_{50}}{10^5} \right] \left[\frac{r_{\text{im}}}{50 \text{ km}} \right]^{1-q} \times \left[\frac{P_i}{2 \times 10^{-22} \text{ km}^2 \text{ yr}^{-1}} \right] \left[\frac{r_{\text{im}} + R_C}{650 \text{ km}} \right] \text{ Gyr}^{-1}, \quad (23)$$

where $N(r, t) \sim r^{1-q}$ is the cumulative size distribution for radius r and time t , q is 3.5–8 as derived from the brightness distribution and dependent on the specific TNO (sub)population (e.g., Petit et al. 2011; Gladman et al. 2012; Shankman et al. 2013, 2016; Adams et al. 2014; Fraser et al. 2014; Schwamb et al. 2014; Alexandersen et al. 2016; Lawler et al. 2018), and P_i is the mean intrinsic probability of collision (Wetherill 1967; Greenberg 1982), which comes from assessments of the distribution of orbit elements of the target and the potential impactors. Our numerical choice for P_i is for collisions between Plutinos and all TNOs (Dell’Oro et al. 2013).

We conclude from Equation (23) that a collision between Charon and an impactor with $r \gtrsim 50$ km is possible over the last few Gyr, with a likelihood at the 10% level. An impact event with a more substantial body, with $r \gtrsim 100$ km, is much less likely. Even with a generously shallow size-distribution slope with $q = 4$, a collision can be ruled out at the 98% level.

Based on these event frequency estimates, a direct hit between Charon and a TNO with a radius $r_{\text{im}} = 50$ km is a plausible origin for the building blocks of the small satellites. However, the model requires a large amount of impact debris compared with the predictions of the cratering scaling law, Equation (22). Greater efficiency in the production of high-speed ejecta remains a possibility, given the uncertainties in a realistic collision between two finite-size spheres (the scaling law strictly applies to a point mass impacting a planar surface). Otherwise, we need to consider alternatives. Potential alternatives include: (i) a smaller impactor with a higher speed than is typical of the Kuiper Belt; (ii) a more efficient way of producing debris with smaller bodies, as in a surface-skimming impact; or (iii) a larger impactor, but at an early epoch when such bodies were more common, with $x_{\text{KB}} \gg 1$. We discuss these cases in turn.

An impactor with radius $r_{\text{im}} = 50$ km and an impact speed of $v_{\text{im}} = 4$ –5 km s^{-1} would produce enough debris to make the satellites, in accordance with the scaling law in Equation (22). However, from the impact speed distributions in Dell’Oro et al. (2013), only about 10% of the potential impactors sustain these high speeds. Thus, the likelihood of Charon encountering a fast-moving smaller body of this size is about the same as the chance of a giant impact with a slower-moving large projectile.

The second possibility is a surface-skimming impact involving a small object ($r_{\text{im}} \lesssim 50$ km) with a highly efficient delivery of mass to the satellite zone. With a smaller mass, we expect less debris, yet an oblique impact can produce a well-directed spray

pattern (e.g., Canup & Salmon 2018). The low probability of getting just the right impact geometry may be balanced by the high abundance of smaller objects. For example, there are five times as many objects with radii greater than 30 km as those with $r_{\text{im}} > 50$ km (for $q = 4$).

Perhaps the most promising avenue is a scenario where the Charon impact happens at an early time, not long after the circularization of the Pluto–Charon binary. Because the Sun’s outer protoplanetary disk was more compact and/or dense during the first ~ 100 Myr of its evolution (e.g., Kenyon 2002; Levison et al. 2008), the primordial Kuiper Belt had many more TNOs than at present. Collisional cascades among TNOs, driven by gravitational stirring (Kenyon & Luu 1999b; Kenyon & Bromley 2004b) or stellar flybys (Kenyon & Bromley 2002), along with dynamical ejections (Morbidelli et al. 2008) and the clearing of small particles by solar radiation and wind, removed more than 99% of the original mass over a period of a billion years (see also Booth et al. 2009). Thus, while collisions with large TNOs are rare today, they were common at early times (Kenyon & Bromley 2014, see Figure 1 and references therein).

If the early Kuiper Belt had a mass that was a hundred times greater than at present, the factor x_{KB} in Equation (23) would be similarly enhanced. Following that equation, and assuming that the timescale for mass loss in the Kuiper Belt is 0.5 Gyr, the likelihood of a collision between Charon and a 100 km TNO is about 30%. It is also ~ 1000 times more likely than the collision that produced the Pluto–Charon binary itself (Kenyon & Bromley 2014). Indeed, the likelihood goes up for other scenarios as well, including the high-speed, lower-mass impactor, and a small, well-aimed surface-skimming TNO.

Whatever the scenario for an impact, Charon is less likely a target than Pluto. From the geometric cross sections alone, an impact on Charon is about 25% as likely as one on its large companion. Gravitational focusing factors do not change this estimate much, since incoming projectiles are typically moving several times faster than the escape speed of either binary partner. Despite Pluto being the larger target, the mass of an impactor would need to be at least an order of magnitude higher to create a reservoir of material in the satellite zone (Figure 3). Given the steep falloff of the size distribution of TNOs, an impact between Pluto and such a large object is less likely than a collision between Charon and a lower-mass projectile.

5.4. Comparison with Other Models

The Charon impactor scenario has one clear advantage over other pictures in which the satellites form from debris produced at that same time as the Pluto–Charon binary. When satellites form during the main Pluto–Charon impact, tidal expansion of the binary pushes destructive resonances through the satellite zone (e.g., Lithwick & Wu 2008a; Cheng et al. 2014b; Smullen & Kratter 2017; Woo & Lee 2018). These resonances probably result in the ejection of at least some of the four satellites. Although this problem can be mitigated if satellites or their precursors are protected from resonant excitation by collisional damping within an circumbinary particle disk (Bromley & Kenyon 2015; Walsh & Levison 2015), this protection must remain in place until the binary has expanded to its present-day orbit. Satellite formation tends to be fast compared with binary expansion (see discussion in Bromley & Kenyon 2015). Thus, this model requires some tuning between the timing of satellite formation and the binary’s orbital expansion.

An impact with another TNO well after the binary expansion finishes, which occurs within the first 1 Myr of the binary’s formation (Cheng et al. 2014a), avoids these difficulties. Pires dos Santos et al. (2012) identify this advantage in proposing a collision between two captured TNOs as a mechanism for producing the satellites. They conclude that this scenario is unlikely, as a result of the short time that these interlopers remain bound to Pluto–Charon. Lithwick & Wu (2008a) explored a similar pathway using a swarm of captured planetesimals in the early solar system.

Since we rely on an impact between the binary and a wayward TNO (see also Petit & Mousis 2004; Parker & Kavelaars 2012; Nesvorný & Vokrouhlický 2019), our model also overcomes the problem of the satellite system’s survival during Pluto–Charon’s tidal evolution. As long as the impact occurs after tidal expansion is complete (~ 1 Myr), but before collisional and dynamical processes have depleted the solar system of TNOs (~ 100 Myr) (Kenyon & Luu 1999b; Kenyon 2002; Levison et al. 2008; Booth et al. 2009; Schlichting & Sari 2011; Schlichting et al. 2013; Kenyon & Bromley 2014), there are sufficient projectiles for an impact and small satellites can grow in an environment where sweeping resonances are not an issue.

Finally, a variant of the scenario presented here involves multiple impacts from more common TNOs with radii of $O(10)$ km or less. The challenge then is for debris particles from each impact to be small and plentiful enough to settle into a circumbinary disk. If low-mass impactors contribute to the growth of the satellites or their precursors in this way, we might expect to see evidence of episodic accretion of small particles onto Nix and Hydra, the largest of the satellites. New Horizons imagery does not provide a compelling case for this scenario, as compared with Cassini observations of Saturn’s moon, Pan, with its pronounced equatorial ridge. However, the complicated spins of the Pluto–Charon moons (Showalter et al. 2019) may well erase that kind of evidence of accretion.

5.5. Observational Consequences of a Charon-impact Origin

The main advantage of a Charon-impact origin for Styx et al. is that their formation occurs after the destabilizing sweeping resonances wrought by the tidal expansion of the binary. Instead, the resonances are at fixed orbital distances. At these locations, disk material is cleared, leaving a gap through which nothing can migrate. It is possible that debris particles can accumulate here and grow through coagulation. Also, by analogy with dynamics in Saturn’s rings (see Crida et al. 2010; Bromley & Kenyon 2013), a satellite may migrate through a field of debris particles. It will likely stop at the edge of a gap, as the supply of solids to drive migration is cut off there. We have simulated exactly this phenomenon in a circumstellar disk with gaps (Bromley & Kenyon 2011b, see Figure 3 therein). We caution that the circumbinary dynamics may be more complicated, involving satellite-satellite interactions, if circumbinary exoplanets are any guide (Sutherland & Kratter 2019).

The cratering record on Charon provides evidence for large impacts in Charon’s distant past (Singer et al. 2019). Careful examination of Charon’s surface reveals evidence for craters (impactors) with diameters as large as 200 km (40 km; see also Schenk et al. (2018)). The largest crater, or other large-scale features like the 450 km dark polar region in Charon’s northern hemisphere, may be the fingerprint of the event that created the satellites.

6. Conclusion

In this “concerto” on the formation and history of the Pluto–Charon binary, we assess the plausibility of an impact between Charon and a large TNO as the origin of the satellite system. Several possibilities generate circumstellar disks with enough mass in the satellite zone to produce the satellites. A direct hit by a 100 km TNO, if treated as a giant cratering event, is likely to eject enough mass to build the satellites. A direct hit by a smaller body, with $r_{\text{im}} = 50$ km, will also work if it efficiently generates ejecta from Charon’s surface. A well-aimed surface-skimming impact by an even smaller, 30 km TNO may also launch enough debris into the satellite zone.

To form a circumbinary disk with enough material to build the satellites, the majority of the mass in the ejecta from the Charon–TNO impact must be in the form of small objects with radii of roughly ten meters or less. Then, collisional damping, accelerated by a collisional cascade, can settle the debris into a long-lived circumbinary disk. Collisions can also capture more widely distributed debris particles into the satellite zone. With our hybrid n -body-coagulation code *Orchestra*, we demonstrate how these processes operate together to concentrate ejected particles into a dynamically cool disk within the satellite zone, truncated beyond Hydra’s orbit.

If most of the ejected mass is in submillimeter-size particles, then a gas cloud with a tenth the mass of the satellites could have entrained the debris. This scenario offers the potential of capturing a large fraction of the impact ejecta, keeping it in the satellite zone. Gravitational settling in the midplane of a circumbinary disk as the gas disperses could result in a reservoir of solids for building the satellites.

Once solid material settles into the dynamically cool disk, collisions and gravity drive satellite growth (Kenyon & Bromley 2014). Specific outcomes depend on uncertain parameters including the surface density profile, particle size distribution, and bulk material properties. Whatever the details, growth is unavoidable; satellites like Styx, Nix, Kerberos, and Hydra are inevitable.

Whether these scenarios are realistic hinges on the likelihood that a large TNO could hit Charon. If a large (~ 100 km) object were needed to provide enough mass for the satellites, the impact must have taken place within the first billion years of the solar system’s history, when such objects were many times more prevalent than they are today. Otherwise, an impact with a smaller (~ 30 – 50 km) body is plausible over the age of the solar system, even with present-day TNO population. Increasing the efficiency of the delivery of mass to the satellite system raises the probability that a small body is responsible.

Exploring these possibilities further requires detailed calculations of the impact (e.g., Arakawa et al. 2019) and the damping process (as in Kenyon & Bromley (2014), with the *Orchestra* coagulation code). Depending on the outcomes of these investigations, the physical properties of the satellites and their orbits may discriminate between models where the satellites are remnants of debris produced during the original giant impact that led to the formation of Pluto–Charon or a somewhat less energetic (but still powerful) collision between a TNO and Charon. One possible discriminant is the proximity of each satellite to a gap-clearing, mean-motion resonance. The pileup of solids near resonances or migration of satellites to gap edges may depend on the origin of debris in the satellite zone and the timing of its placement there relative to the tidal expansion of the binary. Numerical calculations of these

processes may offer a path to choosing among plausible alternatives for the origin of Pluto’s small satellites.

We are grateful to M. Geller for suggestions on our original manuscript. We also thank an anonymous referee for comments that led to further improvements. NASA provided essential support for this work through Emerging Worlds program grant NNX17AE24G and a generous allotment of computer time on the NCCS “Discover” cluster. Binary output files from the simulations and C programs capable of reading them are available at a publicly accessible repository (<https://hive.utah.edu/>) with doi:10.7278/S50D4AKFQZFC.

ORCID iDs

Benjamin C. Bromley  <https://orcid.org/0000-0001-7558-343X>

Scott J. Kenyon  <https://orcid.org/0000-0003-0214-609X>

References

- Adachi, I., Hayashi, C., & Nakazawa, K. 1976, *PThPh*, **56**, 1756
- Adams, E. R., Gulbis, A. A. S., Elliot, J. L., et al. 2014, *AJ*, **148**, 55
- Alexandersen, M., Gladman, B., Kavelaars, J. J., et al. 2016, *AJ*, **152**, 111
- Arakawa, S., Hyodo, R., & Genda, H. 2019, *NatAs*, **3**, 802
- Asphaug, E., Agnor, C. B., & Williams, Q. 2006, *Natur*, **439**, 155
- Benz, W., & Asphaug, E. 1999, *Icar*, **142**, 5
- Bierhaus, E. B., & Dones, L. 2015, *Icar*, **246**, 165
- Booth, M., Wyatt, M. C., Morbidelli, A., Moro-Martín, A., & Levison, H. F. 2009, *MNRAS*, **399**, 385
- Brahic, A. 1975, *Icar*, **25**, 452
- Brahic, A. 1976, *JCoPh*, **22**, 171
- Bridges, F. G., Hatzes, A., & Lin, D. N. C. 1984, *Natur*, **309**, 333
- Bromley, B. C., & Kenyon, S. J. 2006, *AJ*, **131**, 2737
- Bromley, B. C., & Kenyon, S. J. 2011a, *ApJ*, **731**, 101
- Bromley, B. C., & Kenyon, S. J. 2011b, *ApJ*, **735**, 29
- Bromley, B. C., & Kenyon, S. J. 2013, *ApJ*, **764**, 192
- Bromley, B. C., & Kenyon, S. J. 2014, *ApJ*, **796**, 141
- Bromley, B. C., & Kenyon, S. J. 2015, arXiv:1503.06805
- Brozović, M., Showalter, M. R., Jacobson, R. A., & Buie, M. W. 2015, *Icar*, **246**, 317
- Buie, M. W., Grundy, W. M., Young, E. F., Young, L. A., & Stern, S. A. 2006, *AJ*, **132**, 290
- Canup, R., & Salmon, J. 2018, *SciA*, **4**, eaar6887
- Canup, R. M. 2004, *Icar*, **168**, 433
- Canup, R. M. 2005, *Sci*, **307**, 546
- Canup, R. M. 2011, *AJ*, **141**, 35
- Canup, R. M., & Asphaug, E. 2001, *Natur*, **412**, 708
- Cheng, W. H., Lee, M. H., & Peale, S. J. 2014a, *Icar*, **233**, 242
- Cheng, W. H., Peale, S. J., & Lee, M. H. 2014b, *Icar*, **241**, 180
- Crida, A., Papaloizou, J. C. B., Rein, H., Charnoz, S., & Salmon, J. 2010, *AJ*, **140**, 944
- Davis, D. R., Chapman, C. R., Weidenschilling, S. J., & Greenberg, R. 1985, *Icar*, **63**, 30
- Dell’Oro, A., Campo Bagatin, A., Benavidez, P. G., & Alemañ, R. A. 2013, *A&A*, **558**, A95
- Desch, S. J. 2015, *Icar*, **246**, 37
- Doolin, S., & Blundell, K. M. 2011, *MNRAS*, **418**, 2656
- Dvorak, R., Froeschle, C., & Froeschle, C. 1989, *A&A*, **226**, 335
- Foucart, F., & Lai, D. 2013, *ApJ*, **764**, 106
- Fraser, W. C., Brown, M. E., Morbidelli, A. r., Parker, A., & Batygin, K. 2014, *ApJ*, **782**, 100
- Gärtner, S., Gundlach, B., Headen, T. F., et al. 2017, *ApJ*, **848**, 96
- Gaslac Gallardo, D. M., Giulianti Winter, S. M., & Pires, P. 2019, *MNRAS*, **484**, 4574
- Gault, D. E., Shoemaker, E. M., & Moore, H. J. 1963, NASA Technical Note, D-1767
- Gladman, B., Lawler, S. M., Petit, J. M., et al. 2012, *AJ*, **144**, 23
- Goldreich, P., Lithwick, Y., & Sari, R. 2004, *ARA&A*, **42**, 549
- Goldreich, P., & Tremaine, S. 1982, *ARA&A*, **20**, 249
- Greenberg, R. 1982, *AJ*, **87**, 184
- Holman, M. J., & Wiegert, P. A. 1999, *AJ*, **117**, 621
- Holsapple, K. A. 1994, *P&SS*, **42**, 1067

- Housen, K. R., & Holsapple, K. A. 1990, *Icar*, **84**, 226
- Housen, K. R., & Holsapple, K. A. 2011, *Icar*, **211**, 856
- Hyodo, R., Genda, H., Charnoz, S., & Rosenblatt, P. 2017a, *ApJ*, **845**, 125
- Hyodo, R., Rosenblatt, P., Genda, H., & Charnoz, S. 2017b, *ApJ*, **851**, 122
- Kenyon, S. J. 2002, *PASP*, **114**, 265
- Kenyon, S. J., & Bromley, B. C. 2002, *AJ*, **123**, 1757
- Kenyon, S. J., & Bromley, B. C. 2004a, *AJ*, **127**, 513
- Kenyon, S. J., & Bromley, B. C. 2004b, *ApJL*, **602**, L133
- Kenyon, S. J., & Bromley, B. C. 2008, *ApJS*, **179**, 451
- Kenyon, S. J., & Bromley, B. C. 2014, *AJ*, **147**, 8
- Kenyon, S. J., & Bromley, B. C. 2016, *ApJ*, **817**, 51
- Kenyon, S. J., & Bromley, B. C. 2017, *ApJ*, **839**, 38
- Kenyon, S. J., & Bromley, B. C. 2019a, *AJ*, **158**, 142
- Kenyon, S. J., & Bromley, B. C. 2019b, *AJ*, **157**, 79
- Kenyon, S. J., & Bromley, B. C. 2019c, *AJ*, **158**, 69
- Kenyon, S. J., Currie, T., & Bromley, B. C. 2014, *ApJ*, **786**, 70
- Kenyon, S. J., & Luu, J. X. 1999a, *AJ*, **118**, 1101
- Kenyon, S. J., & Luu, J. X. 1999b, *ApJ*, **526**, 465
- Kobayashi, H., & Tanaka, H. 2010, *Icar*, **206**, 735
- Larwood, J. D., & Papaloizou, J. C. B. 1997, *MNRAS*, **285**, 288
- Lawler, S. M., Shankman, C., Kavelaars, J. J., et al. 2018, *AJ*, **155**, 197
- Lee, M. H., & Peale, S. J. 2006, *Icar*, **184**, 573
- Leinhardt, Z. M., & Stewart, S. T. 2009, *Icar*, **199**, 542
- Leinhardt, Z. M., & Stewart, S. T. 2012, *ApJ*, **745**, 79
- Leinhardt, Z. M., Stewart, S. T., & Schultz, P. H. 2008, in *The Solar System Beyond Neptune*, ed. M. A. Barucci et al. (Tucson, AZ: Univ. Arizona Press), 195
- Leliwa-Kopystyński, J., Włodarczyk, I., & Burchell, M. J. 2016, *Icar*, **268**, 266
- Levison, H. F., Morbidelli, A., Vanlaerhoven, C., Gomes, R., & Tsiganis, K. 2008, *Icar*, **196**, 258
- Lithwick, Y., & Wu, Y. 2008a, arXiv:0802.2951
- Lithwick, Y., & Wu, Y. 2008b, arXiv:0802.2939
- Lynden-Bell, D., & Pringle, J. E. 1974, *MNRAS*, **168**, 603
- McKinnon, W. B., Stern, S. A., Weaver, H. A., et al. 2017, *Icar*, **287**, 2
- Melosh, H. J. 1984, *Icar*, **59**, 234
- Melosh, H. J., Ryan, E. V., & Asphaug, E. 1992, *JGR*, **97**, 14735
- Morbidelli, A., Levison, H. F., & Gomes, R. 2008, in *The Solar System Beyond Neptune*, ed. M. A. Barucci et al. (Tucson, AZ: Univ. Arizona Press), 275
- Nakajima, M., & Stevenson, D. J. 2014, *Icar*, **233**, 259
- Nesvorný, D., & Vokrouhlický, D. 2019, *Icar*, **331**, 49
- Nimmo, F., Umurhan, O., Lisse, C. M., et al. 2017, *Icar*, **287**, 12
- O'Brien, D. P., & Greenberg, R. 2003, *Icar*, **164**, 334
- Ohtsuki, K. 1992, *Icar*, **98**, 20
- Ohtsuki, K., Stewart, G. R., & Ida, S. 2002, *Icar*, **155**, 436
- O'Keefe, J. D., & Ahrens, T. J. 1985, *Icar*, **62**, 328
- Ostriker, E. C. 1999, *ApJ*, **513**, 252
- Parker, A. H., & Kavelaars, J. J. 2012, *ApJ*, **744**, 139
- Petit, J.-M., Kavelaars, J. J., Gladman, B. J., et al. 2011, *AJ*, **142**, 131
- Petit, J. M., & Mousis, O. 2004, *Icar*, **168**, 409
- Pires dos Santos, P. M., Giuliatti Winter, S. M., Sfair, R., & Mourão, D. C. 2013, *MNRAS*, **430**, 2761
- Pires dos Santos, P. M., Morbidelli, A., & Nesvorný, D. 2012, *CeMDA*, **114**, 341
- Pitjeva, E. V., & Pitjev, N. P. 2018, *CeMDA*, **130**, 57
- Porco, C. C., Weiss, J. W., Richardson, D. C., et al. 2008, *AJ*, **136**, 2172
- Rafikov, R. R. 2004, *AJ*, **128**, 1348
- Schenk, P. M., Beyer, R. A., McKinnon, W. B., et al. 2018, *Icar*, **315**, 124
- Schlichting, H. E., Fuentes, C. I., & Trilling, D. E. 2013, *AJ*, **146**, 36
- Schlichting, H. E., & Sari, R. 2011, *ApJ*, **728**, 68
- Schwamb, M. E., Brown, M. E., & Fraser, W. C. 2014, *AJ*, **147**, 2
- Shakura, N. I., & Sunyaev, R. A. 1973, *A&A*, **24**, 337
- Shankman, C., Gladman, B. J., Kaib, N., Kavelaars, J. J., & Petit, J. M. 2013, *ApJL*, **764**, L2
- Shankman, C., Kavelaars, J., Gladman, B. J., et al. 2016, *AJ*, **151**, 31
- Showalter, M. R., & Hamilton, D. P. 2015, *Natur*, **522**, 45
- Showalter, M. R., Hamilton, D. P., Stern, S. A., et al. 2011, *IAUC*, **9221**, 1
- Showalter, M. R., Verbiscer, A., Buie, M., & Helfenstein, P. 2019, *AAS/Division of Dynamical Astronomy Meeting*, **51**, 401.02
- Showalter, M. R., Weaver, H. A., Stern, S. A., et al. 2012, *IAUC*, **9253**, 1
- Shuvalov, V. 2009, *M&PS*, **44**, 1095
- Singer, K. N., McKinnon, W. B., Gladman, B., et al. 2019, *Sci*, **363**, 955
- Smullen, R. A., & Kratter, K. M. 2017, *MNRAS*, **466**, 4480
- Stern, S. A., Bagenal, F., Ennico, K., et al. 2015, *Sci*, **350**, aad1815
- Stern, S. A., Grundy, W. M., McKinnon, W. B., Weaver, H. A., & Young, L. A. 2018, *ARA&A*, **56**, 357
- Stoeffler, D., Gault, D. E., Wedekind, J., & Polkowski, G. 1975, *JGR*, **80**, 4062
- Supulver, K. D., Bridges, F. G., & Lin, D. N. C. 1995, *Icar*, **113**, 188
- Sutherland, A. P., & Kratter, K. M. 2019, *MNRAS*, **487**, 3288
- Svetsov, V. 2011, *Icar*, **214**, 316
- Tanaka, H., & Ida, S. 1996, *Icar*, **120**, 371
- Tholen, D. J., Buie, M. W., Grundy, W. M., & Elliott, G. T. 2008, *AJ*, **135**, 777
- Walsh, K. J., & Levison, H. F. 2015, *AJ*, **150**, 11
- Ward, W. R., & Canup, R. M. 2006, *Sci*, **313**, 1107
- Weaver, H. A., Buie, M. W., Buratti, B. J., et al. 2016, *Sci*, **351**, aae0030
- Weaver, H. A., Stern, S. A., Mutchler, M. J., et al. 2006, *Natur*, **439**, 943
- Weidenschilling, S. J. 1977, *MNRAS*, **180**, 57
- Wetherill, G. W. 1967, *JGR*, **72**, 2429
- Wetherill, G. W., & Stewart, G. R. 1993, *Icar*, **106**, 190
- Whipple, F. L. 1972, in *From Plasma to Planet*, ed. A. Elvius (New York: Wiley), 211
- Williams, D. R., & Wetherill, G. W. 1994, *Icar*, **107**, 117
- Woo, J. M. Y., & Lee, M. H. 2018, *AJ*, **155**, 175
- Youdin, A. N., Kratter, K. M., & Kenyon, S. J. 2012, *ApJ*, **755**, 17